B3 3rd Year Group Project Report

Project 3:

A new beam-profile monitor for the Large Hadron Collider at CERN

Ben Brown (BB)

Matthew Budd (MB)

Philippe Rottner (PR)

FINAL HONOUR SCHOOL OF ENGINEERING SCIENCE

DECLARATION OF AUTHORSHIP

You should complete this certificate. It should be bound into your third year project report, immediately after your title page. Three copies of the report should be submitted to the Chairman of examiners for your Honour School, c/o Clerk of the Schools, examination Schools, High Street, Oxford.

Name (in capitals): BEN BROWN

College (in capitals): JESUS **Supervisor(s):** Dr Alice Cicirello, Dr Daniel Eakins

Title of project (in capitals): A NEW BEAM-PROFILE MONITOR FOR THE LARGE HADRON COLLIDER AT CERN

Page count (excluding risk and COSHH assessments): 30

Please tick to confirm the following:

I have read and understood the University's disciplinary regulations concerning conduct in examinations and, in particular, the regulations on plagiarism (*The University Student Handbook. The Proctors' and Assessors' Memorandum, Section 8.8*; available at https://www.ox.ac.uk/students/academic/student-handbook) ☐

I have read and understood the Education Committee's information and guidance on academic good practice and plagiarism at https://www.ox.ac.uk/students/academic/guidance/skills. ☐

The project report I am submitting is entirely my own work except where otherwise indicated. ☐

It has not been submitted, either partially or in full, for another Honour School or qualification of this University (except where the Special Regulations for the subject permit this), or for a qualification at any other institution. ☐

I have clearly indicated the presence of all material I have quoted from other sources, including any diagrams, charts, tables or graphs. ☐

I have clearly indicated the presence of all paraphrased material with appropriate references. ☐

I have acknowledged appropriately any assistance I have received in addition to that provided by my supervisor. ☐

I have not copied from the work of any other candidate. ☐

I have not used the services of any agency providing specimen, model or ghostwritten work in the preparation of this project report. (See also section 2.4 of Statute XI on University Discipline under which members of the University are prohibited from providing material of this nature for candidates in examinations at this University or elsewhere: http://www.admin.ox.ac.uk/statutes/352-051a.shtml.) ☐

My contribution to the joint report does not exceed 30 pages (including all diagrams, photographs, references and appendices). ☐

I agree to retain an electronic copy of this work until the publication of my final examination result, except where submission in hand-written format is permitted. ☐

I agree to make any such electronic copy available to the examiners should it be necessary to confirm my word count or to check for plagiarism. ☐

Candidate's signature: …….. **Date:** ……..

FINAL HONOUR SCHOOL OF ENGINEERING SCIENCE

DECLARATION OF AUTHORSHIP

You should complete this certificate. It should be bound into your third year project report, immediately after your title page. Three copies of the report should be submitted to the Chairman of examiners for your Honour School, c/o Clerk of the Schools, examination Schools, High Street, Oxford.

Name (in capitals): MATTHEW BUDD

College (in capitals): PEMBROKE **Supervisor(s):** Dr Alice Cicirello, Dr Daniel Eakins

Title of project (in capitals): A NEW BEAM-PROFILE MONITOR FOR THE LARGE HADRON COLLIDER AT CERN

Page count (excluding risk and COSHH assessments): 30

Please tick to confirm the following:

I have read and understood the University's disciplinary regulations concerning conduct in examinations and, in particular, the regulations on plagiarism (*The University Student Handbook. The Proctors' and Assessors' Memorandum, Section 8.8*; available at https://www.ox.ac.uk/students/academic/student-handbook) ☐

I have read and understood the Education Committee's information and guidance on academic good practice and plagiarism at https://www.ox.ac.uk/students/academic/guidance/skills. ☐

The project report I am submitting is entirely my own work except where otherwise indicated. ☐

It has not been submitted, either partially or in full, for another Honour School or qualification of this University (except where the Special Regulations for the subject permit this), or for a qualification at any other institution. ☐

I have clearly indicated the presence of all material I have quoted from other sources, including any diagrams, charts, tables or graphs. ☐

I have clearly indicated the presence of all paraphrased material with appropriate references. ☐

I have acknowledged appropriately any assistance I have received in addition to that provided by my supervisor. ☐

I have not copied from the work of any other candidate. ☐

I have not used the services of any agency providing specimen, model or ghostwritten work in the preparation of this project report. (See also section 2.4 of Statute XI on University Discipline under which members of the University are prohibited from providing material of this nature for candidates in examinations at this University or elsewhere: http://www.admin.ox.ac.uk/statutes/352-051a.shtml.) ☐

My contribution to the joint report does not exceed 30 pages (including all diagrams, photographs, references and appendices). ☐

I agree to retain an electronic copy of this work until the publication of my final examination result, except where submission in hand-written format is permitted. ☐

I agree to make any such electronic copy available to the examiners should it be necessary to confirm my word count or to check for plagiarism. ☐

Candidate's signature: …….. **Date:** ……..

FINAL HONOUR SCHOOL OF ENGINEERING SCIENCE

DECLARATION OF AUTHORSHIP

You should complete this certificate. It should be bound into your third year project report, immediately after your title page. Three copies of the report should be submitted to the Chairman of examiners for your Honour School, c/o Clerk of the Schools, examination Schools, High Street, Oxford.

Name (in capitals): PHILIPPE ROTTNER

College (in capitals): EXETER **Supervisor(s):** Dr Alice Cicirello, Dr Daniel Eakins

Title of project (in capitals): A NEW BEAM-PROFILE MONITOR FOR THE LARGE HADRON COLLIDER AT CERN

Page count (excluding risk and COSHH assessments): 16

Please tick to confirm the following:

I have read and understood the University's disciplinary regulations concerning conduct in examinations and, in particular, the regulations on plagiarism (*The University Student Handbook. The Proctors' and Assessors' Memorandum, Section 8.8*; available at https://www.ox.ac.uk/students/academic/student-handbook) ☐

I have read and understood the Education Committee's information and guidance on academic good practice and plagiarism at https://www.ox.ac.uk/students/academic/guidance/skills. ☐

The project report I am submitting is entirely my own work except where otherwise indicated. ☐

It has not been submitted, either partially or in full, for another Honour School or qualification of this University (except where the Special Regulations for the subject permit this), or for a qualification at any other institution. ☐

I have clearly indicated the presence of all material I have quoted from other sources, including any diagrams, charts, tables or graphs. ☐

I have clearly indicated the presence of all paraphrased material with appropriate references. ☐

I have acknowledged appropriately any assistance I have received in addition to that provided by my supervisor. ☐

I have not copied from the work of any other candidate. ☐

I have not used the services of any agency providing specimen, model or ghostwritten work in the preparation of this project report. (See also section 2.4 of Statute XI on University Discipline under which members of the University are prohibited from providing material of this nature for candidates in examinations at this University or elsewhere: http://www.admin.ox.ac.uk/statutes/352-051a.shtml.) ☐

My contribution to the joint report does not exceed 30 pages (including all diagrams, photographs, references and appendices). ☐

I agree to retain an electronic copy of this work until the publication of my final examination result, except where submission in hand-written format is permitted. ☐

I agree to make any such electronic copy available to the examiners should it be necessary to confirm my word count or to check for plagiarism. ☐

Candidate's signature: …….. **Date:** ……..

Table of Contents

BB: MB: PR:

Table of Figures

1 INTRODUCTION, RESEARCH AND PROJECT DEFINITION

1.1 Project Background and Context

CERN has been at the centre of nuclear physics for the last 30 years and is constantly striving to find new ways to improve their research. They are currently in the process of upgrading the Large Hadron Collider (LHC) to create the High Luminosity-LHC (HL-LHC). This 950 million Swiss Franc upgrade aims to provide scientists with more data than ever before by increasing the luminosity, number of potential collisions per unit surface area for a given period of time, by a factor a 10. One of the key parts of the upgrade will be the use of more powerful quadrupoles and the new “crab cavities” which are used to focus and manipulate the proton beams so that they overlap inside the experiments [1][2].

To optimize the use of these new technologies in the HL-LHC, CERN would like to have an accurate idea of the beam shape and position. This information can then be used by the “crab cavities” to maximise the luminosity and therefore increase the amount of data produced by the experiments. It would be ideal if the information is updated in real time or at least with a very small integration time. Since the protons are travelling at almost the speed of light, a small integration time ensures that they do not travel too far after having been measured. This will prove crucial if a beam is to be altered in real time. A beam profile monitor can be used to fulfil both of these criteria, however, there are some constraints.

One of CERN’s main objectives is that the chosen system does not interfere with the proton beam. Previous technologies include wire scanners which consist of a wire being repeatedly moved up and down across the proton beam. The interaction of the wire with the proton beam causes a “shower of secondary particles” which are detected by scintillators outside of the beam pipe before becoming an electrical signal using photo-multiplier tubes. The intensity of the electrical signal is plotted against the position of the scanner to give a transverse beam profile [3]. This process is destructive to the wire and after a short period it would be destroyed. Once the HL-LHC has started up CERN intends to keep it running for several months at a time, if not years. Any repairs are extremely costly and require a full shut-down of the HL-LHC hence the need for a system which is non-invasive.

In addition to this, the instrumentation cannot influence the shape of the beam or introduce contaminating particles into the vacuum. This means that electric or electromagnetic fields should not be used as they might have an effect on the proton beams.

1.2 Beam-Induced Fluorescence Gas Curtain Beam Profile Monitor: Principles

A new non-invasive technology CERN is interested in using is called beam induced fluorescence (BIF). The basic principle that is being exploited is that of de-excitation where an electron that goes from a higher energy level to a lower one will emit the energy difference in the form of light.

The main method is to fire a “curtain” of gas across the trajectory of the beam. These gas molecules may then be hit by protons and cause some of the energy of the collision to excite an electron into a higher energy level. The curtain is sent at 45° across the particle beam this enables it to act like a mirror. The light from the subsequent de-excitation can then be captured by a camera or charged coupled device (CCD).

The emission of light due to excitation can occur in any random direction from a molecule which is not ideal as it means our CCDs may not detect any light. This is a shortcoming of the system which limits the received power.

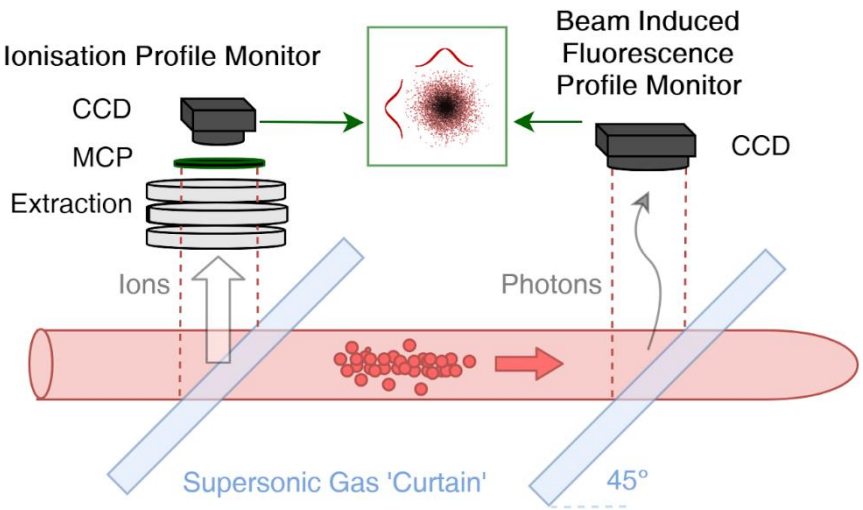

Figure 1: Diagram of BIF Monitor [from final presentation, MB]

1.3 Literature Review

An in-depth literature review was carried out in early Michaelmas. The four papers below were chosen for summary in this section, as together they outline the main aspects of a beam induced fluorescence profile monitor and highlights the development of this technology over the past decade.

"Beam induced fluorescence profile monitor developments (2010) [4]"

A paper reviewing the general performance of the new beam induced fluorescence technology, developed at the GSI heavy ion facility. It studies the fluorescence spectra of nitrogen and other possible working gases.

"Gas dynamics considerations in a non-invasive profile monitor for charged particle beams (2016) [5]"

A paper by the QUASAR group at the Cockcroft Institute concentrating on the problems associated with small nozzle and subsequent skimmer dimensions. It deals with the dynamics of gas jet formation and proposes a possible image-processing based alignment technique. There is also a focus on the effects of the gas column's stagnation pressure.

"Characterizing supersonic gas jet-based beam profile monitors (2016) [6]"

A paper by the Cockcroft Institute demonstrating the supersonic gas jet monitor's superior resolution and signal to noise ratio in comparison to a residual gas profile monitor. It also uses ion drift simulation to further analyse the resolution of this monitor.

"Design and first operation of a supersonic gas jet based beam profile monitor (2017) [7]"

A paper by the Cockcroft Institute presenting a more complete picture of the beam profile monitor. It describes in detail the nozzle and skimmer configuration to generate a supersonic gas jet and highlights its use as a versatile and universal beam profile monitor that can be implemented for any beam type.

1.4 Business Case

To understand this business case, it is first essential to look at the purposes and goals of CERN. To appeal to CERN, as a project of great interest and possible further work, a project must aid these purpose and goals. Below are what CERN describe as their mission [8]:

- *Provide a unique range of particle accelerator facilities that enable research at the forefront of human knowledge.*
- *Perform world-class research in fundamental physics.*
- *Unite people from all over the world to push the frontiers of science and technology, for the benefit of all.*

The first point makes it clear that CERN are in the business of particle accelerators. This is evident in section 1.1 and is the obvious purpose for better understanding and optimising this BIF monitor.

The second point is more of a challenge to achieve on face value. However, it can be understood that facilitating, rather than performing, world-class research in fundamental physics is just as important. This therefore means that working on elements of the BIF monitor that are present in other systems at CERN would be very beneficial. Another perspective would be proving the reliability of a concept, as due to CERN's limited human resources, showing that a part of an apparatus works consistently allows for their human resources to be used more effectively elsewhere. For example, to focus on performing the world-class research in fundamental physics that they wish to do.

The third point refers to the global outlook of CERN and their desire for multinational collaborations. This means that outsourcing is often encouraged, leading to looking for the best manufacturing processes globally rather than solely looking for local or cheap sources.

1.5 Projects and Approaches Considered

The literature review confirmed that a gas curtain was a sensible approach to profiling the particle beam, and that our project goal should be to improve an aspect of the BIF-based profile monitor.

One area investigated for a potential 3rd Year Project was the formation of the gas curtain from a gas jet: this is a key area for the profile measurement instrument as the performance of the gas curtain depends highly on the attributes of the gas jet that it is formed from.

Another technical issue identified in the literature review and discussion with CERN involved the choice of gas species for the curtain. Nitrogen is in many ways a very good candidate gas, and has a particularly high photon emission cross section (i.e. it would emit far more photons than noble gases such as neon, improving the signal-to-noise ratio). However, photons are far more likely to be emitted from nitrogen ions (also formed by particle beam collisions) than neutral N_2, and the large electrical and magnetic fields in the beamline would accelerate these ions. As the half-life of nitrogen to emit a photon after a particle collision is ~60 ns, during this time the ion would be accelerated and displaced which would cause a measurement error.

Two possible project proposals were put together and pitched to CERN via video call on 30/10/2018:

1. **Fluid flow analysis for the gas apparatus**: this would involve investigating and optimising the formation of the gas curtain via the gas jet, mainly focusing on the nozzle and skimmers that collimate the gas jet. The result of this project would be more analysis/information on the gas apparatus and design suggestions for improving its performance.
2. **Space charge analysis**: this would involve analysing and modelling the fields inside the beamline chamber to try to account for nitrogen ion movement before photon emission. The result of this project would be an algorithm to correct the raw images from the CCD, by extrapolating backwards to remove the effect of molecule displacement before emission.

Option 1 was chosen as our 3rd Year Project. Both projects were shown to be of interest to CERN in the project proposal video call, but option 1 was considered to be more achievable in the time available as well as being more suited to the varied skillsets of our project team.

1.6 Project Planning and Management

Reference management was implemented with a Mendeley shared repository, where all relevant literature was stored. Document (report, meeting minutes and presentations) version control and coordination were implemented through a shared Google Drive. As CERN was effectively the “client”, the project was focused on technical research, analysis and design rather than a full business-case engineering study: for example, economic feasibility analysis (B2) was not applicable. The project timeline plan (including key dates) was drawn up and agreed on 05/11/2018.

1.6.1 Project Key Dates

- **10/2018-11/2018:** Phase 1: Literature review, concept generation and project choice.
- **11/2018-04/2019:** Phase 2: Detail design and analysis, completion of most project work.
- **04/2019-05/2019:** Phase 3: Final write-up, presentations and report submission.
- **30/10/2018, 20/11/2018, 22/01/2019, 26/02/2019:** Presentations to CERN via video call.
- **23-24/04/2019:** Trip to CERN in Geneva to present results and acquire feedback.

1.6.2 Technical Work Breakdown and Report Structure

The project team had a wide range of skills based on their chosen modules: BB’s modules included mechanical engineering and fluid dynamics, PR’s modules included electronic/information engineering and thermodynamics, and MB’s modules included electronic/information and control engineering. This report is presented in several technical sections and one final conclusion section:

Section 2 (BB) examines the usage of a combination of one-dimensional compressible flow relations and CFD software to model, analyse and propose possible improvements to the compressible flow region of the gas jet.

Section 3 (PR) examines undesirable flow effects in the gas jet and curtain, how these may impact the performance of the gas apparatus and how these effects may be mitigated. Undesirable flow effects include condensation and clusters of particles that may impact measurements or the vacuum.

Section 4 (MB) discusses the development of a gas jet model for the molecular flow regime.

Section 5 (MB) details the development of a proposed experimental instrument to validate computer models of the gas flow, which (as discussed in other sections) are key to gas apparatus design.

2 COMPRESSIBLE FLOW: THEORY, ANALYSIS AND LIMITATIONS

2.1 Current Compressible Flow Set Up

2.1.1 Background

This section of the project will encompass the parts of the BIF monitor within the compressible flow regime. It will also explore the boundary between the compressible flow regime and the molecular flow regime with the aim of determining at which point in the system the laws of compressible flow break down. In physical terms, this means this section will analyse the output of the pressurised canister which holds the working gas; the nozzle that accelerates the gas to high Mach numbers; the first chamber which the working gas enters after leaving the nozzle; and the skimmer which takes off the central column of gas and is the boundary between the first and second chamber, shown in figure 2 and figure 3 [9].

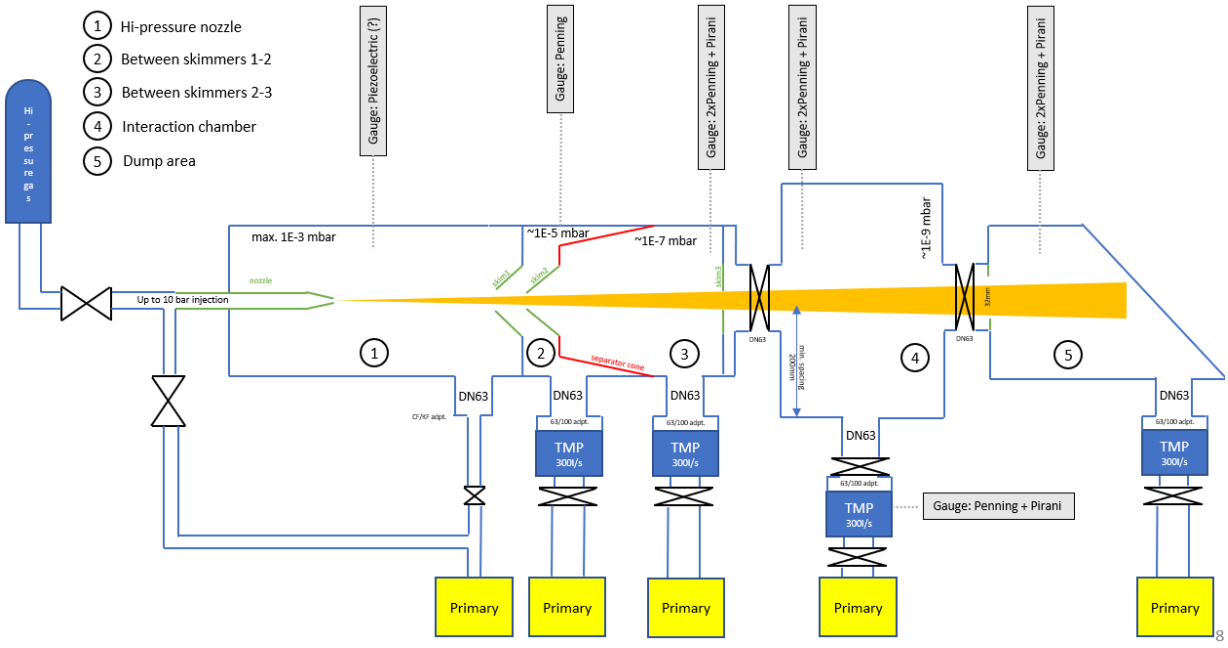

Figure 2: Schematic of BIF monitor.

Figure 3: Schematic of BIF monitor only showing the relevant parts to this section.

The aim of the discussion is to assess the current situation and to produce insight into possible amendments.

In this, the first sub-section (2.1), the constraints on the system will be outlined and a brief study of the solid mechanics of certain parts of the apparatus will be studied. There will also be an initial look into the theory of Knudsen number which defines the flow regime. This will help define and challenge the boundaries of compressible flow.

The second sub-section (2.2) will introduce convergent-divergent (CD) nozzles and the one-dimensional equations associated with them. It will mainly deal with the manipulation of the non-dimensional ratios in these equations. The aim here will be to understand the trade-offs resulting from these equations and hence provide a tool for selecting a CD nozzle area ratio.

The third sub-section (2.3) will use the same equations but will come at the problem from a different angle; i.e. aiming to design a CD nozzle with as close to optimal results as possible, as set out above, yet also achieving "design condition". This is that the pressure at the exit of the nozzle equals the ambient pressure in the first chamber, and hence produces streamlines in the first chamber parallel to one another. Therefore, the values associated with the flow are independent of position along the central axis of the first chamber. This setup will greatly simplify the system, therefore making analysis and implementation of the position of the first skimmer relative to the nozzle significantly easier. This section will also include CFD analysis to supplement understanding.

All of the equations relating to fluid flow in this section (section 2) will assume that the flow regime is compressible flow. This was done firstly to supplement the current understanding of the compressible flow regime and highlight the challenges of doing so, and secondly to complement the work on molecular flow in section 4.

2.1.2 Constraints

As the aim here is to provide a useful service to CERN, this section will work to pre-defined constraints to allow realistic implementation of the suggestions made in this report. The schematic from CERN (figure 2 and figure 3) has many of the constraints annotated on it. For this section, the notable values are: a maximum of 1 MPa inlet pressure; a maximum of 0.1 Pa first chamber pressure; and a second chamber pressure of the order of 1 mPa (see table 1).

The nozzle, being a very specialised part, is currently a concentric one manufactured by Rutherford Appleton. From email correspondence with Rutherford Appleton, it was clear that the main constraint would be that the smallest hole possible for their machining apparatus is 30μm diameter. This means that any nozzle suggested must at its narrowest cross-section be no less than 30μm in diameter [10].

For the first skimmer, a depiction in figure 4 is provided based on a thorough description in the literature [7], where in practice the image is rotated 90 degrees anti-clockwise and the flow is from left to right. The most important detail here is the initial opening being 200μm in diameter.

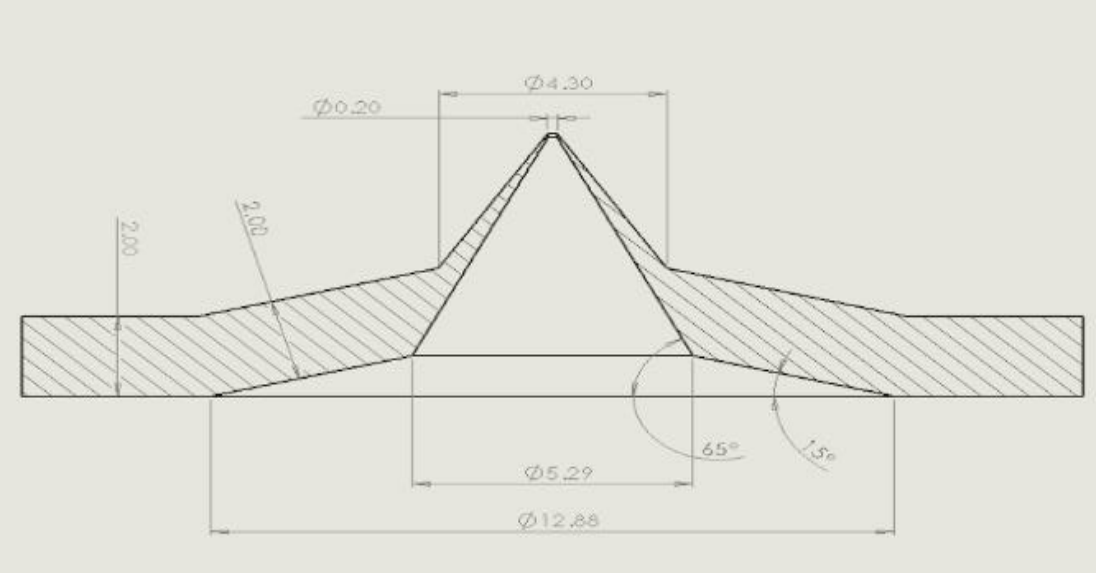

Figure 4: Side cut through of first skimmer (all values in mm).

For the purposes of this section, table 1 lays out the five constraints with which all calculations work within.

Maximum nozzle inlet pressure	1 MPa
Maximum first chamber pressure	0.1 Pa
Second chamber pressure	1 mPa
Minimum diameter of nozzle	30 μm
Diameter of first skimmer	200 μm

Table 1: Summary of constraints.

The choice of working gas receives a lot of attention in the literature [4]. It seems that the two most favoured gases are nitrogen and neon. In a group discussion, it was decided that it appears that CERN are leaning towards the use of nitrogen; hence, unless otherwise stated its associated material properties will be used in all parts of this report (table 2).

Property	**Value**
Molecular weight (MW)	28.01 $kg.kmol^{-1}$
Gas constant (R)	0.297 $kJ.kg^{-1}.K^{-1}$
Ratio of specific heat capacities (γ)	1.40
Molecular diameter (d_m) [11]	370 pm
Thermal conductivity at s.t.p.* (k)	24.3 $mWm^{-1}.K^{-1}$
Dynamic viscosity at s.t.p.* (μ)	17.4 μPa.s
Specific heat capacity at constant pressure, for s.t.p.* (C_p)	1.039 $kJ.kg^{-1}.K^{-1}$

*s.t.p. refers here to a pressure of 1atm (1.013 bar) and temperature of 0 ^oC

Table 2: Properties of nitrogen [12].

2.1.3 Stress Analysis of Skimmer

In this section a structural analysis of the current skimmer is explored. This was undertaken largely as a safety measure to make sure that there were no unexpected deviations from the desired set up. For this it was decided that the large mass of material (i.e. lack of sheet metal) meant that it would not be necessary to undertake a stress analysis of the nozzle. In contrast, the skimmer is

made of, in part, thin sheets of metal. This intuitively suggests that a basic stress analysis of the skimmer might be a worthy endeavour.

To do this, the skimmer was drawn up in SolidWorks, as shown in figure 4, and then analysed with SolidWorks inbuilt static analysis software, a type of Finite Element Analysis (FEA) software. A static analysis was chosen due to the nature of the apparatus, which will be operational for long periods of time, and therefore would reach equilibrium conditions, and hence can be modelled as a static system. The FEA covers the geometry in triangles to make up the mesh to be analysed. The mesh was refined to be finer around the tip of the skimmer and coarser further away, as shown in figure 5. This was to increase the resolution around the area of greater interest. The material selected was copper as indicated in the literature [7].

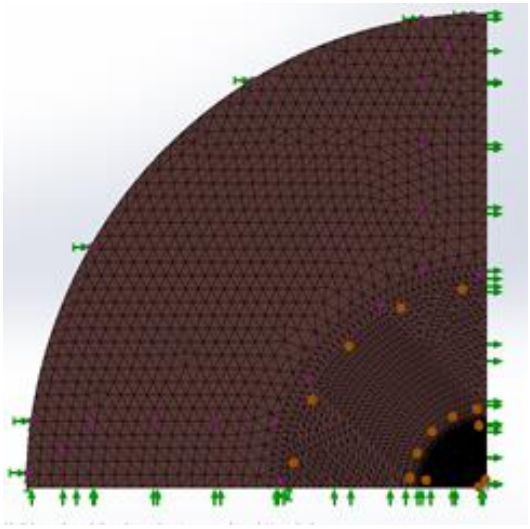

Figure 5: Meshed quarter segment of skimmer front on with increased resolution around the tip.

As the skimmer is symmetric radially, a quarter segment was used for analysis as this provides significant computational efficiency savings with no negative implications on results. The two cut-through sides of the skimmer were set to be "mirrored" to help the system accurately predict a full skimmer. The outer section of the skimmer, which is perpendicular to fluid flow, was set as "fixed" as this section can be manufactured to a much greater thickness, if required, without adversely affecting fluid flow. To initialise the software, a circular pressure field over the full surface of the skimmer was input in the direction of fluid flow.

As stated in section 2.1.2, the most important value associated with the skimmer is the 200 μm diameter and hence this was the focus of this static simulation.

The results of this study were that even for the highest conceivable pressure on the skimmer, being 1 MPa, the diameter of the inlet to the skimmer deformed by less than 0.1 μm. This puts the skimmer

diameter as correct to ±0.05% when in operation. To emphasise how low this value is, this is smaller than the tolerance to which the machining process at Rutherford Appleton can work to [10].

2.1.4 Knudsen Number

The Knudsen number (*Kn*) is a dimensionless value that describes the state of the flow. Whether the flow is continuous and therefore compressible, or whether it is molecular flow.

$$Kn = \frac{\bar{L}}{d} \qquad \text{(Eqn. 1)}$$

Where $\bar{L}$ is the mean free path (m), and *d* is the diameter of the flow channel (m).

$$\bar{L} = \frac{kT}{\sqrt{2}\pi P {d_{\mathrm{m}}}^2} \qquad \text{(Eqn. 2)}$$

Where *k* is the Boltzmann constant ($J.K^{-1}$), and *T* is the free steam temperature (K), *P* is the static pressure (Pa), and d_m is the molecular diameter (m).

There is some debate as to the exact boundary at which compressible flow breaks down and molecular flow begins. However, the method of "The Vacuum Technology Book" [13], which is the source for figure 6 and equations 1 and 2, introduces an intermediate flow regime calling it "Knudsen flow" referring to 0.01 < Kn < 0.5. Larger values refer to molecular flow, and smaller values refer to compressible flow. An alternative definition is that the intermediate flow regime refers to 0.01 < Kn < 0.1 [14].

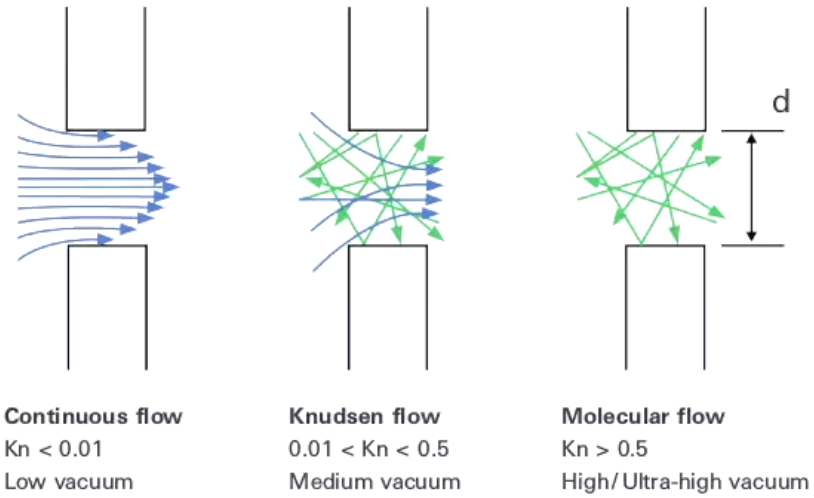

Figure 6: Depiction of flow regime based on Kn no. [13]

Using the above definition of Knudsen number, it is interesting to note that for the conditions in the first chamber, being T = 10 K and P = 0.1 Pa [15], the fluid is considered molecular flow for all diameters of the flow channel below 4.5 mm. To be considered compressible flow the diameter of flow channel would need to be more than 230 mm.

This very much challenges the understood assumption of CERN that the flow in the first chamber is compressible flow. However, as other types of flow are beyond the scope of this section (molecular flow is considered in section 4), the rest of this section has used compressible flow equations as a reasonable basis on which to explore the validity of various amendments.

2.2 Converging-Diverging Nozzle Trade Offs

2.2.1 Acknowledgement of Previous Work

The current nozzle, and all available alternatives set out in the literature [7], follow the same pattern of allowing an uncontrolled expansion of gas into the first chamber, followed by the centre-line column being tapped off by the first skimmer. The logic to this being that what happens to the particles outside of the central column is irrelevant, as only the central column will continue down the apparatus.

In this section, the possibility of using a CD nozzle will be explored in terms of trade-offs (section 2.2) and later with a greater focus on the shape of the expansion (section 2.3). It is noted that the notion of using a CD nozzle is not foreign to this problem, as seen in the presentation to CERN by Przemysław Smakulski, from the University of Wroclaw. In this, Smakulski demonstrated CD nozzles to be superior to through-hole nozzles but did not deal with the somewhat uncontrolled nature of the gas expansion [15].

2.2.2 Equations of Compressible flow

The following understanding of the equations governing compressible fluid flow at and above the speed of sound come predominantly from the B19 course and notes provided by Professor Colin Wood (including the source of equations 3 and 4).

Equations relating to a CD nozzle:

$$\frac{T_0}{T} = \left(\frac{P_0}{P}\right)^{\frac{\gamma-1}{\gamma}} = \left(\frac{\rho_0}{\rho}\right)^{\gamma-1} = 1 + \frac{\gamma-1}{2}M^2 \quad \text{(Eqn. 3)}$$

$$\frac{A_2}{A_1} = \frac{M_1}{M_2}\left(\frac{1+\frac{\gamma-1}{2}M_2^2}{1+\frac{\gamma-1}{2}M_1^2}\right)^{\frac{\gamma+1}{2(\gamma-1)}} \quad \text{(Eqn. 4)}$$

Where the positions of the *T* temperature (K), *P* pressure (Pa) and ρ density (kg.m^{-3}) terms in equation 3 are shown in figure 7 and M Mach number refers to the exit Mach number. Equation 4 refers to the cross-sectional area ratio (hereby referred to as area ratio) at a point where the flow is supersonic but most commonly refers to the cross-sectional area at the throat (A_t) and the cross-sectional area at the exit (A_e). γ is the ratio of specific heat capacities. Note: equation 3 can be viewed as a relation between Mach number and temperature, with the added clauses simply a result of including the isentropic relations between temperature, pressure and density.

To achieve equations 3 and 4, several idealisations have been made. These are that the system is frictionless, steady, one-dimensional, isentropic, adiabatic, and that a perfect gas is used.

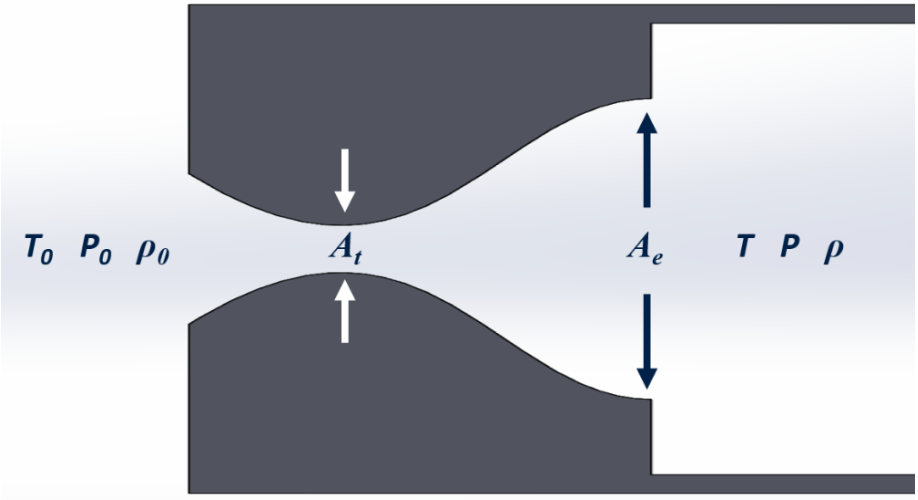

Figure 7: Convergent-Divergent nozzle.

2.2.3 Dimensionless Optimisation Approach

An initial approach was to see this as an optimisation problem where the variables in equations 3 and 4 could either be increased or decreased to achieve an optimal outcome. A closer look at the variables available to us shows that this problem can be simplified to a three-way design task of Mach number versus area ratio versus temperature ratio or pressure ratio or density ratio, shown

more clearly below. This is because the ratio of specific heat capacities is predefined, and pressure, density and temperature are all related through the perfect gas equation of state, equation 5.

$$M \quad \text{vs.} \quad \frac{A_e}{A_t} \quad vs. \quad \frac{T_0}{T} \text{ or } \frac{P_0}{P} \text{ or } \frac{\rho_0}{\rho}$$

$$P = \rho RT \qquad \text{[16] (Eqn. 5)}$$

Where P is pressure (Pa), ρ is density (kg.m^{-3}), R is gas constant (J.kg^{-1}.K^{-1}) and T is temperature (K).

Working with the value ratios (and Mach number in the case of speed), rather than their absolute terms, has the benefit of keeping all calculations dimensionless, which makes it applicable to the full range of absolute values. It also makes the trade-offs easier to understand, as many of the values will range from zero to one, rather than a value that is only understood in the context of each data set.

To further narrow down the three-way design task, from the variables in the perfect gas equation of state, it was decided that density ratio was to be the focus. Density can be described as the average number of particles in any given area at a moment in time. Downstream of the nozzle, in the LHC, this value needs to be high enough to allow for enough interactions to produce photons for the detector. Therefore, the density in the centre line stream out of the nozzle needs to be maximised. It could be argued that density should not be maximised, rather it should be at an optimal value. However, due to possible losses of particles further down the apparatus not studied in this section of the project, and the absolute values produced being on the lower side, the density ratio will be set to be maximised to try to achieve an absolute value as close as possible to what may be desired. This decision was made based on a group discussion and was later validated in section 4.4.1 when it was found that only ~1% of the working gas reaches the LHC chamber. Note: From here on in, normalised density ratio will refer to density at exit over density at entrance to nozzle ($\frac{\rho}{\rho_0}$).

Mach number, being effectively a normalised velocity term as shown in equation 6, can be understood as the velocity term in the direction along the apparatus. Each particle will have a small component of random velocity due to its temperature defined by the Maxwell-Boltzmann equation,

discussed in section 4.3.3, and shown in equation 13. The ideal is for all the particles to travel in the direction along the apparatus. However, the velocity of a particle is the sum of the velocity components from Mach number and from the temperature component, where the former is in the desired direction, and the latter is not. Mach number is therefore to be maximised with the to aim to get it to dominate the overall velocity equation.

$$M = \frac{V}{\alpha} \quad \text{[17] (Eqn. 6)}$$

$$\alpha = \sqrt{\gamma RT} \quad \text{[18] (Eqn. 7)}$$

Where M is Mach number, V is velocity (m.s^{-1}), α is the speed of sound (m.s^{-1}), γ is the ratio of specific heat capacities, R is gas constant (J.kg^{-1}.K^{-1}) and T is temperature (K).

The third variable in the three-way design task, area ratio, will therefore be the independent variable. Figure 8 is a plot of area ratio against Mach number and area ratio against the normalised density. It can therefore be seen that to maximise Mach number, the area ratio needs to be minimised. However, to maximise normalised density, the area ratio needs to be maximised. These optimisations are achieved through opposite activities therefore a decision regarding the importance of large Mach number versus large normalised density needs to be made.

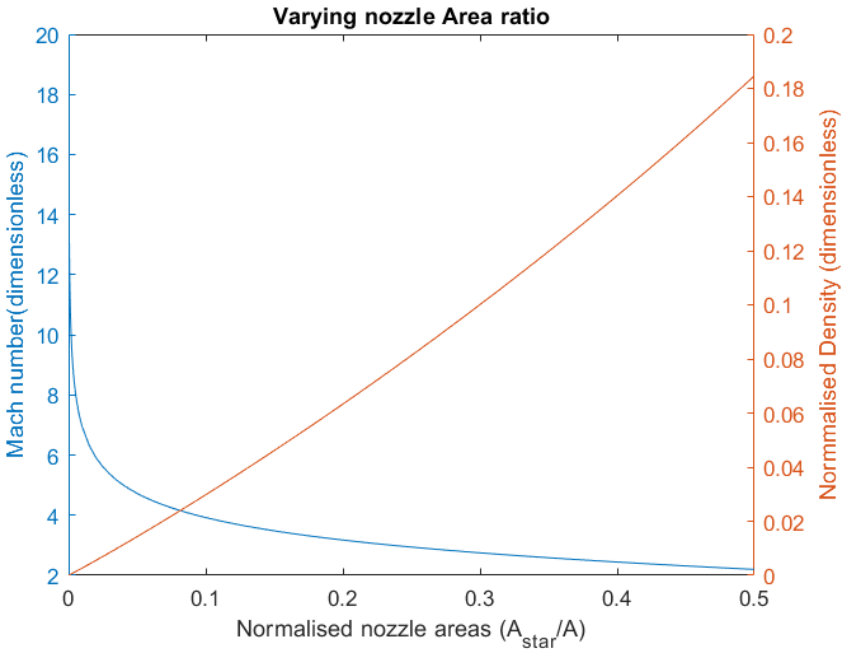

Figure 8: Plot of Mach no. and Normalised Density where both are to be maximised.

This decision is one for CERN to make, therefore figure 9 shows a variety of different weightings of Mach number versus normalised density to illustrate the matter. Due to the nature of the relationships between area ratio, normalised density and Mach number respectively, when weighted equally the optimal area ratio is 0.99. If, for example, Mach number was deemed three times as important as density, the optimal area ratio would be 0.31.

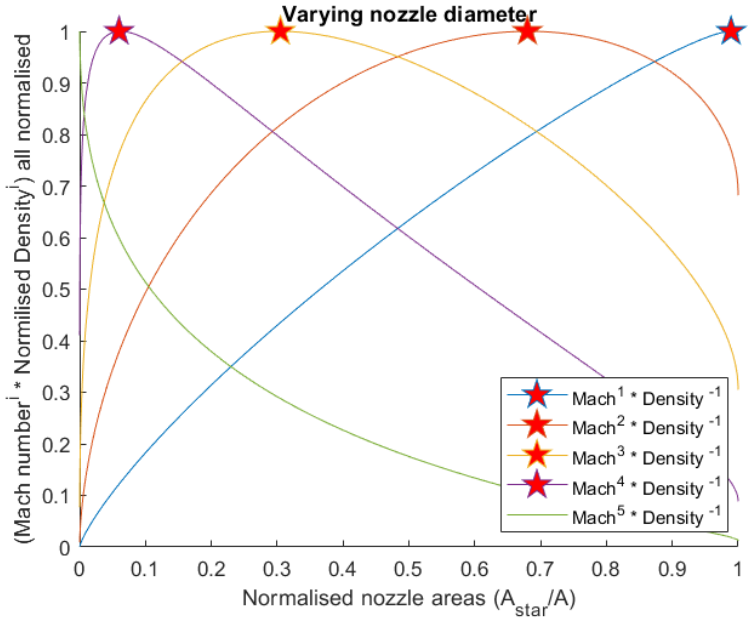

Figure 9: Plot of different optimum Area ratios depending on the importance of Mach no. relative to Normalised Density.

2.3 Converging-Diverging Nozzle Pressure Matching

2.3.1 One Dimensional Approach

Section 2.2 studies the numerical values associated with the nozzle and provides a useful grounding in the basic trends of compressible flow. However, it does not deal with the direction of the streamlines of fluid flow out of the nozzle. In this section, using a combination of one-dimensional hand calculations with the assistance of MATLAB, and the CFD software ANSYS Fluent to model a more realistic two-dimensional model, the direction of the streamlines will be analysed.

The aim will be to achieve perfectly horizontal streamlines out of the nozzle in the direction of the skimmer, to provide optimal directional flow downstream through the apparatus.

The flow through a CD nozzle can be categorised into seven situations, illustrated in figure 11. In this figure and for the purposes of this study, it is useful to talk in terms of pressure. However, it would be equally correct to talk in terms of Mach number, which would produce graphs flipped along the horizontal axis intersecting the point of inflection of (F) and will be done so when appropriate. The plots in figure 11 describe the following types of flow.

A) Subsonic flow

B) Flow just choked

C) shock in nozzle

D) shock at exit

E) over expanded

F) design condition

G) under expanded

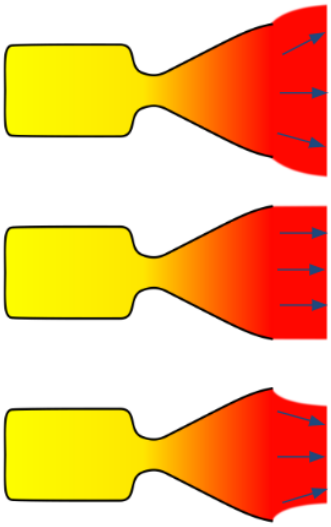

Figure 10: Fully developed expansions with arrows denoting the direction of the streamlines as they leave the nozzle. Top to Bottom: Under expanded, Design condition, Over expanded [19].

(G) is the category within which all the current nozzles operate. (F) is the design condition this project aims to achieve illustrated in figure 10.

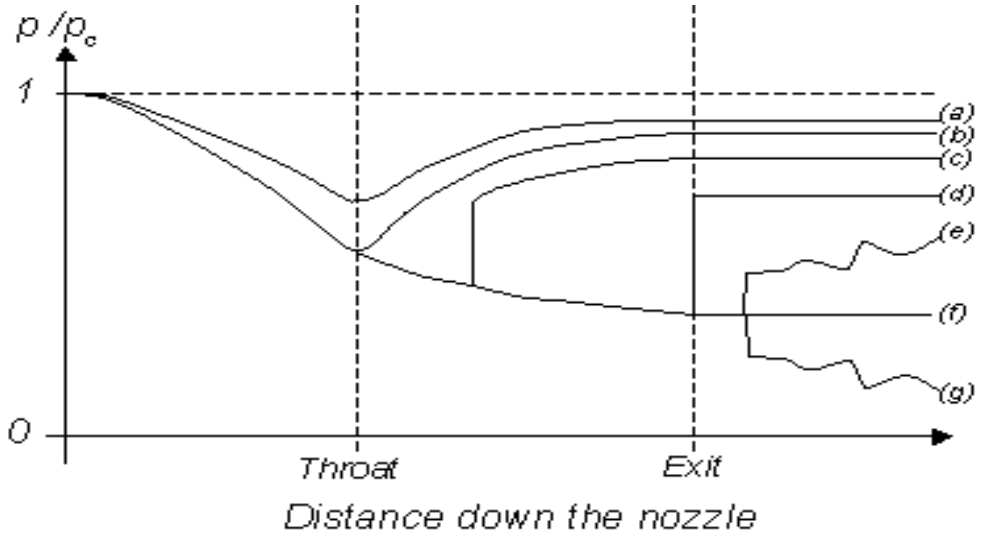

Figure 11: Plot of Pressure ratio along the central axis of the nozzle for the seven flow categories [20].

To achieve design condition, is it first essential to ensure that the flow reaches Mach 1 at or before the throat. This is achieved through having a small throat relative to inlet cross sectional area. The analysis will focus on CD nozzles with throat diameter of 30 μm, which makes designing an inlet area sufficiently large an easy task, hence requiring no further discussion.

The ambient pressure at the outlet of the nozzle is essential for achieving design condition. As demonstrated in figure 11 if the nozzle exit pressure is too low relative to the ambient pressure, over expansion will occur. This is the process of flow going through oblique shockwaves in order to match exit pressure with ambient pressure, and hence the flow will converge towards the centreline. However, if the pressure is too high, under expansion will occur. This is a process of flow going through expansion fans to match the exit to ambient pressure. Both processes will destabilize the flow, hence producing a non-uniform flow. The challenge therefore is to produce a system where the exit pressure equals the ambient pressure.

Using MATLAB, equations 3 and 4 were implemented for the full range of inlet pressures, 0-1 MPa, given a throat diameter of 30 μm and output pressure of 0.1 Pa, to produce the exact output diameter that will produce design condition for each inlet pressure, as shown in figure 12.

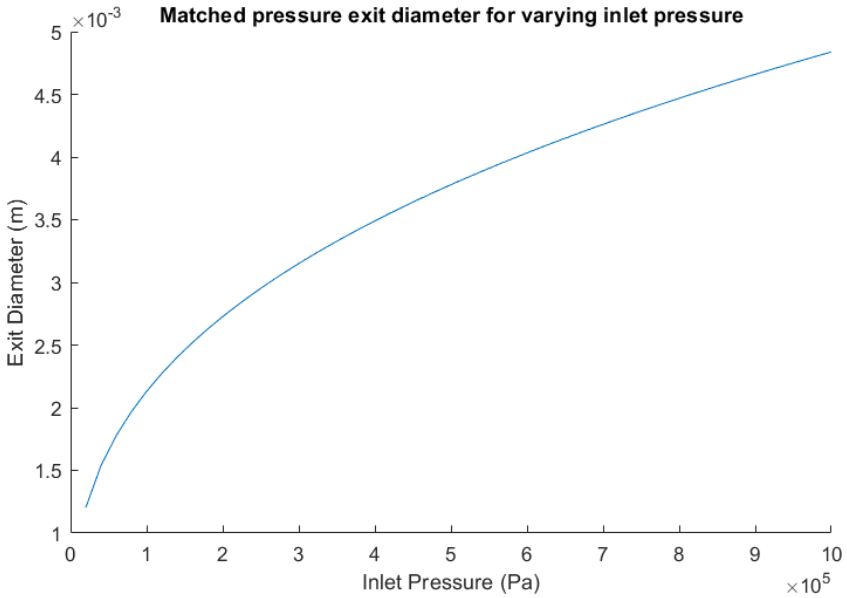

Figure 12: Plot of Inlet Pressure against Exit Diameter for the minimum 30 μm Throat Diameter, to achieve design condition.

Table 3 shows the values associated with a 1MPa inlet pressure.

	Variable	Value
Predefined in table 1	Inlet pressure (P_0)	1 MPa
	Outlet pressure (P)	0.1 Pa
	Throat diameter (D_t)	30 µm
	Inlet Temperature (T_0)	300 K
Results from equations 3 and 4	Mach number (M)	22.2486
	Density ratio ($\frac{\rho}{\rho_o}$)	$1x10^{-5}$
	Pressure ratio ($\frac{P}{P_o}$)	$1x10^{-7}$
	Temperature ratio ($\frac{T}{T_o}$)	$1x10^{-2}$
	Area ratio ($\frac{A}{A_t}$)	26011
Application of Area ratio	Exit diameter (D)	4.8 mm
	Outlet Temperature (T)	3 K

Table 3: Full set of values for design condition with predefined pressures and throat diameter.

To further understand this setup a simulation in ANSYS Fluent was created with the specification laid out in table 3.

2.3.2 Computational Analysis

2.3.2.1 Initialisation

To create the required geometry, a text file of points outlining a Mach 1.5 nozzle from the "B19 transonic nozzle lab (CFD)" was imported into Microsoft Excel and then adapted to conform with the desired specification. ANSYS ICEM was then used to create a mesh shown in figure 13, with special care being required to ensure minimal warping of cells.

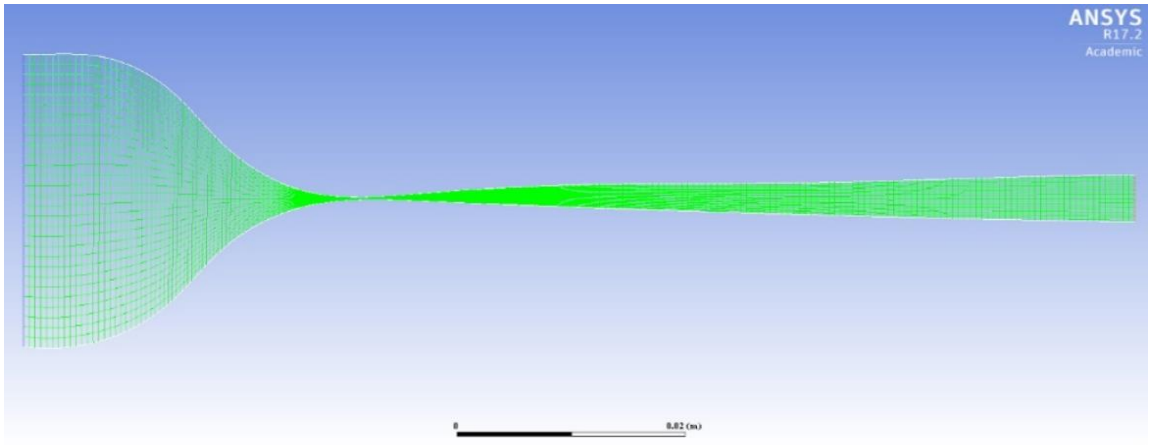

Figure 13: Meshed 2-Dimentional CD nozzle with dimensions driven by table 3.

For computational efficiency and ease of use, the model is two-dimensional. The idea is that the full nozzle will be symmetrical, rotating 180° about its central horizontal axis. It therefore would seem necessary to only compute half of nozzle and set a symmetry boundary along its central axis. However, as discussed later, for minimal extra computation work, there is good reason to model both halves.

Table 4 describes the parameters set in the ANSYS Fluent model:

Geometry	Inlet diameter 30 mm to ensure Mach 1 is reached at the throat demonstrated in figure 13, throat diameter 30 μm and an exit diameter 4.8 mm as calculated in table 3 to ensure pressure matching.
Fluid properties	All the relevant material properties of nitrogen were inputted as laid out in table 2.
Time	Steady - as this apparatus will be in use for long periods at a time.
Solid properties	Zero displacement of walls which was deemed a fair assumption.
Iterations of solution	A solution converged at around 120 iterations hence leaving the pre-advertised number of iterations at 300 was a safe precaution.
Flow Courant number	It is used to stabilise the convergence of a solution and is initially set to 200. Due to the large pressure drops and mesh area difference of high order of magnitude, to produce a solution the flow Courant number was set to 100.

Table 4: Details of ANSYS Fluent Solver.

2.3.2.2 Results

Nozzle Centre line

The middle plot of figure 14 shows the distribution of pressure along the central horizontal axis of the nozzle. This closely matches that of (F) from figure 11, showing that this computational set up accurately portrays a design condition CD nozzle.

It does however produce an exit Mach number of 4.3, which requires further attention as this deviates greatly from, Mach 22, the value produced in the one-dimensional equations (equations 3 and 4).

Figure 14 also includes the variation of static temperature. These three plots together are the data required for the analysis in section 3 to determine the chances of cluster formation and/or condensation.

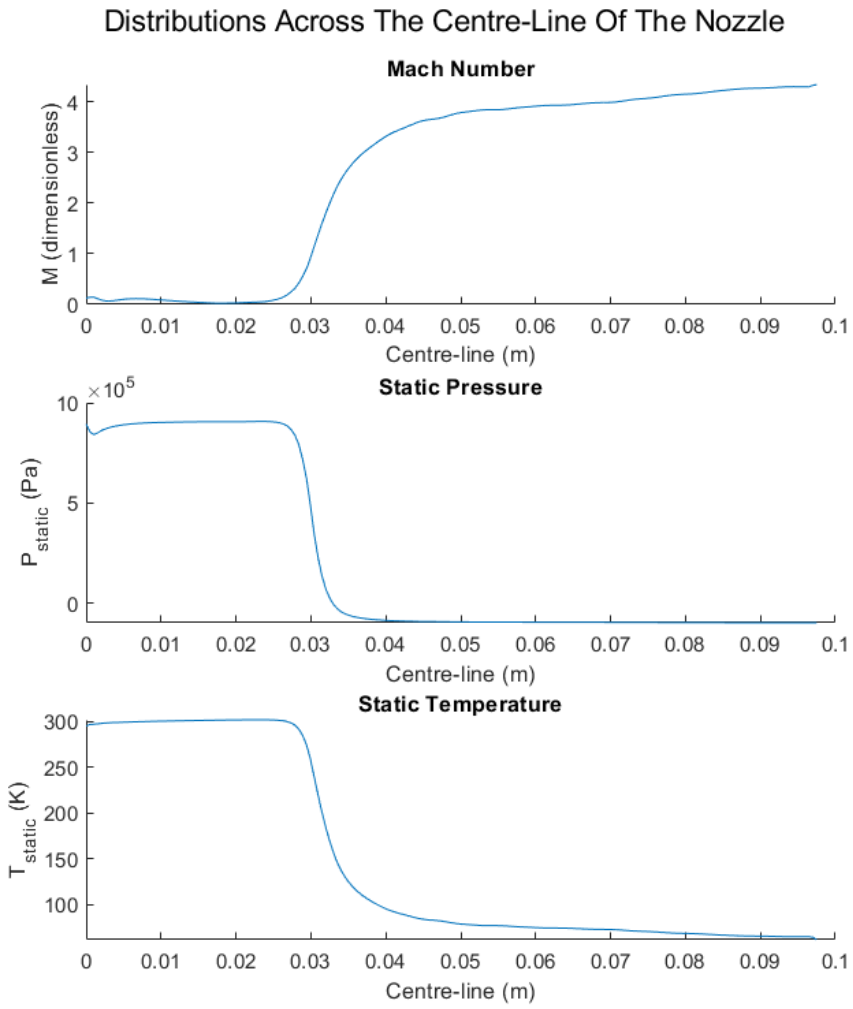

Figure 14: Top to bottom: Distribution of Mach no., Static Pressure, and Static Temperature along the central axis on the nozzle.

Nozzle Exit

The most relevant section of the data produced in the CFD model is that at the exit of the nozzle. This is because it will directly shape the flow downstream. As indicated above, this setup was designed to produce uniform flow, specifically flow in which the streamlines are parallel. As such, it is fair to assume, and essential for the purposes of collaboration between this section and section 4, that the values associated with the flow at the exit of the nozzle are unchanged through the first chamber and can be used as the inputs to the first skimmer. To further highlight the relevant values, in figures 15, 16 and 18, and orange and red lines indicate the central 200μm which will feed into the skimmer opening. Hence the distributions in the areas in between these two lines are reproduced with higher resolution for use in the model in section 4.

The values associated with the CFD model that can be compared with the one-dimensional compressible flow equations results are those in the central peaks, or central troughs, as these will be the least affected by separation and wall friction. This is in line with the findings of other researchers, an example being the study of a Mach 1.6 nozzle [21], hence the presence of these peaks and troughs is expected in the case studied in the CFD model, due to its much larger Mach number.

Mach number

The hand calculations in table 3 indicate an output Mach number of 22 which, is considerably larger than that shown in figure 15 (top left), being Mach 4.3. As seen in equation 6, the Mach number is a function of velocity and the speed of sound. From figure 15(bottom left), the centreline horizontal velocity is 705 $m.s^{-1}$, which is very close to the value yielded from the hand calculation, that being 786 $m.s^{-1}$. This therefore indicates that the problem lies with the speed of sound.

The speed of sound is a function of the universal gas constant, the ratio of specific heat capacities, and the static temperature shown equation 7. Figure 15 (top and bottom right) validates that it is the

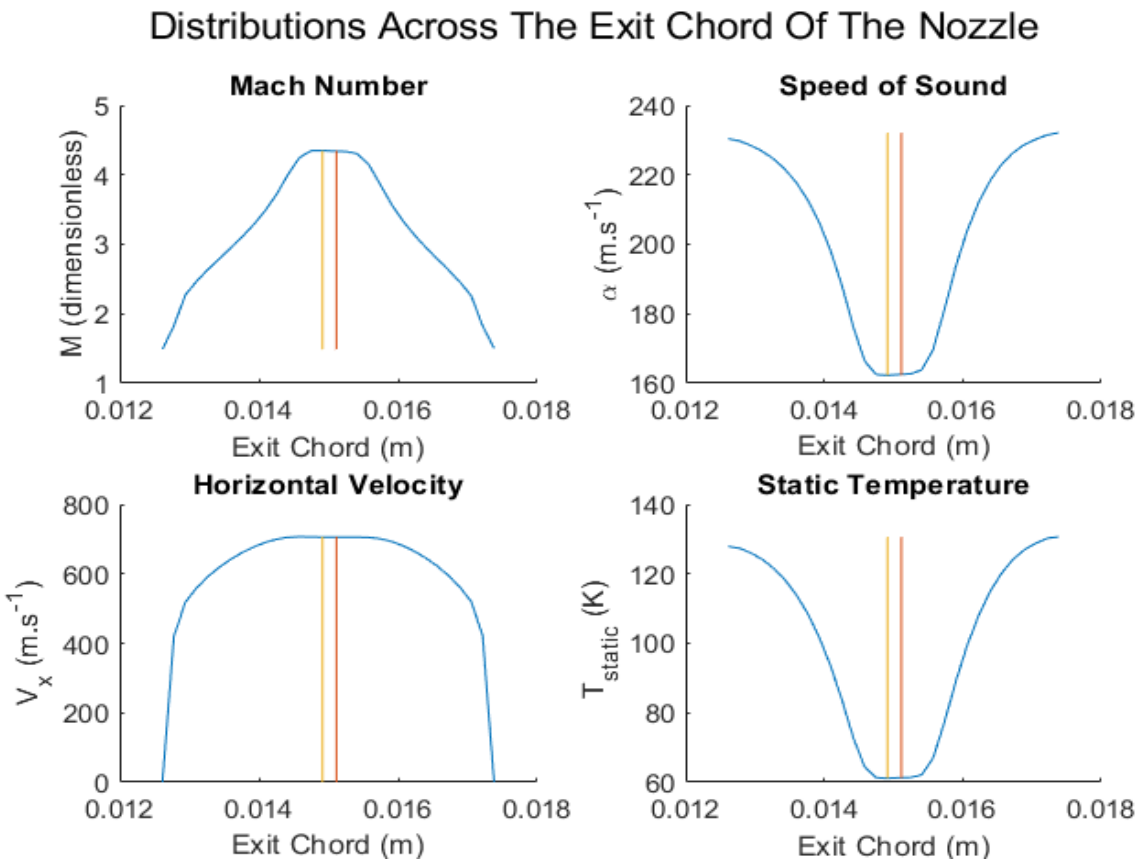

Figure 15: Distribution of all the component variable of Mach no. across the exit of the nozzle. Orange and red lines denote the central 200 µm. Clockwise from top left; Mach no., speed of sound, horizontal velocity, and static temperature.

static temperature with which the speed of sound varies, as the graph for the speed of sound distribution mirrors that of static temperature in shape. This gives an indication of where the inconsistency in Mach number stems from. In figure 15 (bottom right), the static temperature trough is at 61 K, whereas the hand calculations yield a value of 3 K.

The most probable reason for this discrepancy is due to the idealisations used in the hand calculations. It is also worth noting that almost all material [21] [22], using these equations are for relatively low Mach numbers indicative of lower speeds. These lower speeds allow for the neglect of frictional effects, which if included, logically raises the static temperature.

In summary this discrepancy in Mach number is not necessarily a problem, as the reason such a large Mach number was desired, was to have a large horizontal velocity. As shown above, even though in the CFD model the Mach number is significantly lower, the horizontal velocity is only minimally affected.

Vertical velocity

As stated earlier, it would seem logical to only compute half of this nozzle. However, computing both halves shows an interesting phenomenon of a vertical velocity, shown in figure 16. This led to further investigation into whether this was common for CD nozzles, or whether there was some error in the software or its input/application.

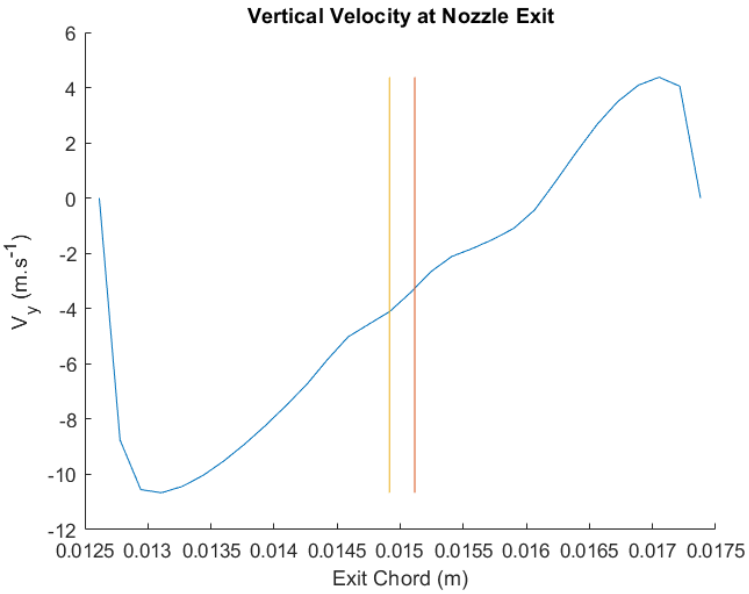

Figure 16: Distribution of vertical velocity across the exit of the nozzle. Orange and red lines denote the central 200 µm.

It was subsequently discovered through the literature on Mach 1.6 [21] and Mach 2 [22] nozzles, that these non-ideal behaviours are to be expected. Interestingly, the vertical velocity component in each of their tests was consistent in direction for the duration of the experimental test but varied randomly with each experimental test. Unsurprisingly, however, each simulation completed for this study in ANSYS Fluent yielded the same horizontal velocity distribution, as depicted in figure 17.

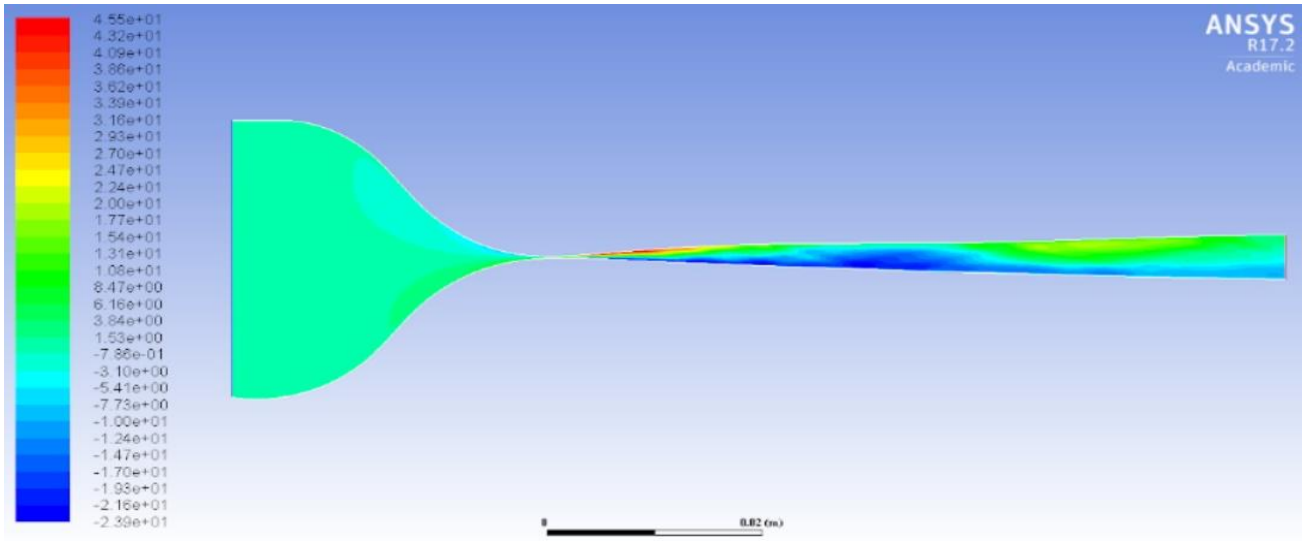

Figure 17: Colour plot of nozzle depicting vertical velocity (colour scale units are in m.s^{-1}).

2.3.2.3 Comparison to Previous Work

As previously mentioned, Smakulski has done significant work on CD nozzles, trying out a variation of geometries and inlet pressures to find the optimal configuration [15]. On slide 13 of his presentation, he collates his results in two graphs, one being horizontal velocity versus position along the centre line, and the other being density verses position along the centre line. From these graphs, it is shown that the best configuration that he tested was a CD nozzle of divergent length 2 mm with an inlet pressure of 3 bar. This yielded a velocity of ~ 600 m.s^{-1} and a density of 1×10^{23} m^{-3}.

Comparing these results to that of the nozzle tested in this section shows that both in terms of density and velocity, the nozzle tested in this section was superior Smakulski's. To do a simple comparison for density, a conversion of units was necessary, from the peak value in figure 18, using the molecular weight of nitrogen (table 2) and Avogadro's number [12] as shown below.

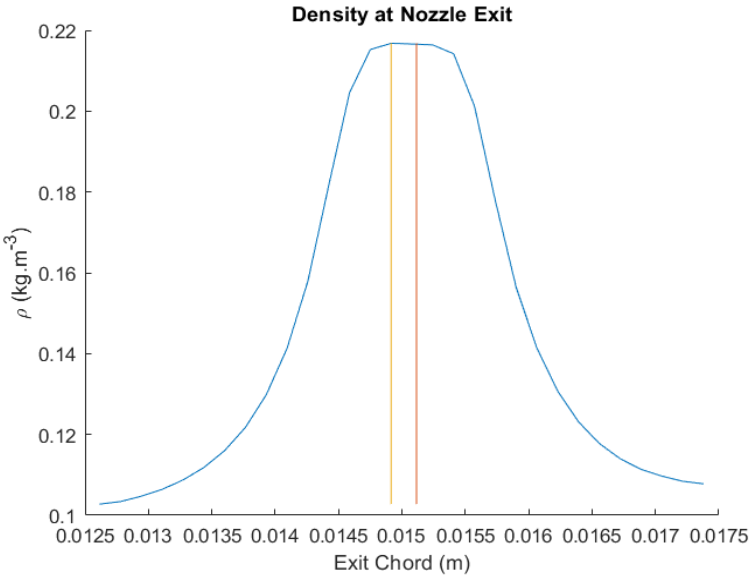

Figure 18: Distribution of density across the exit of the nozzle. Orange and red lines denote the central 200 μm.

$$\rho_{N_2}[kg.m^{-3}] \times \frac{N[Kmol^{-1}]}{MW_{N_2}[kg.Kmol^{-1}]} = \rho_{no.\ density}[m^{-3}]$$

$$0.217[kg.m^{-3}] \times \frac{6.022 \times 10^{26}[Kmol^{-1}]}{28.01[Kg.Kmol^{-1}]} = 4.67 \times 10^{24}[m^{-3}]$$

Smakulski's Nozzle	Nozzle tested in this section
$\rho = 1 \times 10^{23}\ m^{-3}$	$\rho = 4.67 \times 10^{24}\ m^{-3}$
$V = 600\ m.s^{-1}$	$V = 705\ m.s^{-1}$

Table 5: Comparison of Smakulski's to nozzle in this section with regards to density and velocity.

Table 5 shows that the velocity is 17.5% greater and the density over 10 times greater for the nozzle tested in this section, compared to that tested by Smakulski. It is however worth noting that Smakulski also modelled the expansion into the first chamber and hence his is a more accurate representation of the full system.

2.3.3 Knudsen Number Based on Results

As shown in equations 3 and 4, for a given chamber pressure and working gas, the only independent variables are temperature and diameter of flow channel. Table 6 shows the results for the temperatures from the one-dimensional hand calculations, literature [15], and the CFD software, for both the nozzle exit and the skimmer.

Temperature	Knudsen no. for Nozzle Exit (d = 4.8mm)	Knudsen no. for Skimmer (d = 200µm)
3 K (1D equation)	0.14 - Knudsen Flow	3.4 - Molecular Flow
10 K (value from papers)	0.47 - Knudsen Flow	11.3 - Molecular Flow
61 K (ANSYS Fluent)	2.98 - Molecular Flow	71.5 - Molecular Flow

Table 6: Knudsen no. for the nozzle exit and skimmer entrance for three different temperature situations.

From this, it is clear why using conventional methods of compressible flow analysis yield somewhat peculiar results. None of the Knudsen numbers produced indicate a compressible flow regime. Furthermore, the compressible flow solver, ANSYS Fluent, indicated that the flow that it was analysing was in fact fully molecular flow.

2.3.4 Application to First Skimmer

As the initial understanding was that it was ambiguous as to whether it was compressible or molecular flow at the skimmer, the idea of modelling the skimmer as just the divergent part of a CD nozzle was considered. A basic not to scale picture was drawn in SolidWorks, shown in figure 19. This, in theory, would work as a further expansion with the skimmer exit at 200 μm.

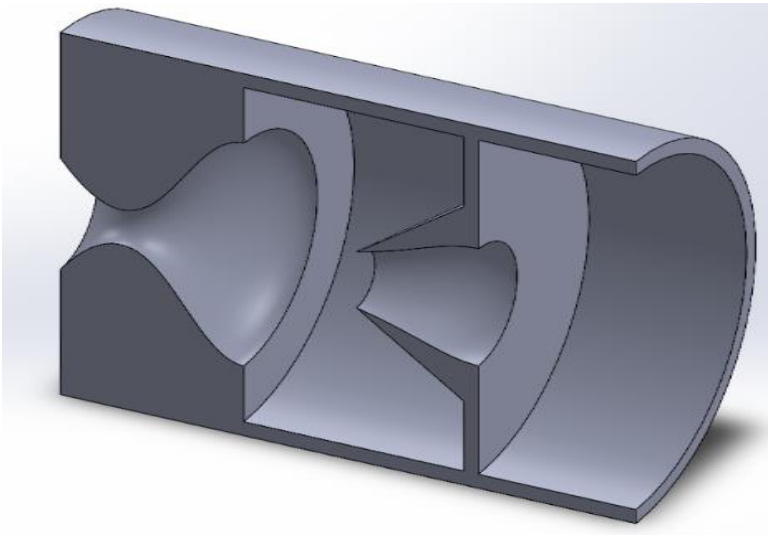

Figure 19: Initial design idea for applying CD theory to both the nozzle and the skimmer.

Apart from the fact section 2.3.3 demonstrates that the skimmer is in molecular flow, the mathematics involved in producing pressure matched expansions yield geometries that do not fit together. To set this out, the following analysis was carried out with values from table 1.

Equation 3 suggests that the difference in first and second chamber pressures results in a Mach 3.7 expansion. Equation 4 therefore indicates that the inlet to the skimmer would need to be 35.7 mm. This is impossible, as the nozzle exit is only 4.8 mm, therefore constraining the skimmer inlet to a maximum of 4.8 mm.

The above evidence suggests that another approach is required to study the flow through the first skimmer. This will be undertaken in section 4.

3 UNDESIRABLE FLOW EFFECTS: THEORY AND ANALYSIS

3.1 Background and Justification

A major concern in the generation of the supersonic gas jet is condensation or clusters. Condensation is when a gas turns into a liquid or when it turns into solid crystals. Clusters are much smaller than the droplets formed through condensation, typically $<10^6$ molecules in size, and these will usually be formed due to Van der Waals forces. Clusters are also what form at the very beginning of condensation.

The presence of condensation or clusters poses a real threat to the integrity of the testing equipment and vacuum used at CERN. Large particles moving at high speeds will have a relatively large momentum and therefore could cause damage to equipment being used. CERN usually runs for months or even years at a time: any shut-down of the HL-LHC is incredibly costly and also a waste of time as not only will equipment need to be replaced, but the vacuum needs to be re-established.

The main phenomenon being exploited for the BIF profile monitor is the de-excitation of electrons which in turn will emit light. The presence of other droplets or clusters means that light may not be emitted when required or not at all. Light from de-excitation will be emitted in a random direction, and as a result of this the light may be emitted from an atom into a neighbouring atom in the same cluster. This could occur multiple times within the same cluster as it travels in the direction of the gas curtain so that when an actual excitation is then detected it could be much further away than the point of original excitation.

As clusters are propagated along the gas jet there is a risk that they break apart as they approach the proton beam, which means that there will be a higher density of gas molecules at that point. This is not ideal as it would mean an increase in density in random areas throughout the gas curtain. This might yield more light emittance in a certain area simply due to the fact that there are more particles which can collide.

3.2 Condensation

3.2.1 Basics

In the simplest of cases condensation occurs when the combined pressure and temperature of an element is above the saturation line. This may lead to either the formation of droplets of liquid or simply solid crystals. Phase diagrams provide a visual representation of where different states occur.

3.2.2 Phase Diagrams

A phase diagram has temperature on the horizontal axis and pressure on the vertical axis and it is assumed that the volume is kept constant. It can be used to work out exactly what phases are present. Saturation lines are used to denote a clear boundary between the different states of matter: solid, liquid and gas.

There are two points of interest on a phase diagram: the critical point and the triple point. The critical point is the maximum of liquid-vapour equilibrium. Any point above the critical temperature can no longer be compressed into a liquid, it simply becomes a highly compressed gas. The critical temperature is dependent on the strength of attraction between particles, the higher the intermolecular forces the higher the critical temperature. The triple point is when all three phases meet in equilibrium and occurs at a unique pressure and temperature. The triple point can also be thought of as the point where three saturation lines meet: the solid-vapour equilibrium line, solid-liquid equilibrium line and the liquid-vapour equilibrium line [23].

The following are phase diagrams for the two working fluids that we have been considering, Neon and Nitrogen. The data for figure 20 and figure 21 has been found from [24] and [25].

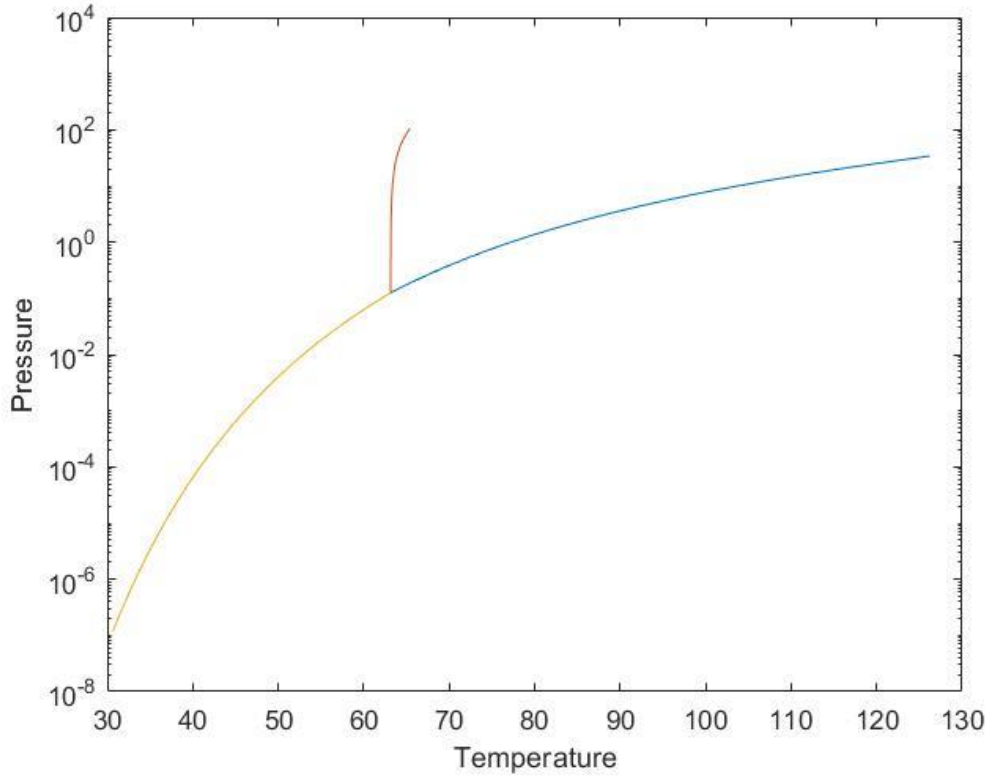

Figure 20: Phase diagram of nitrogen.

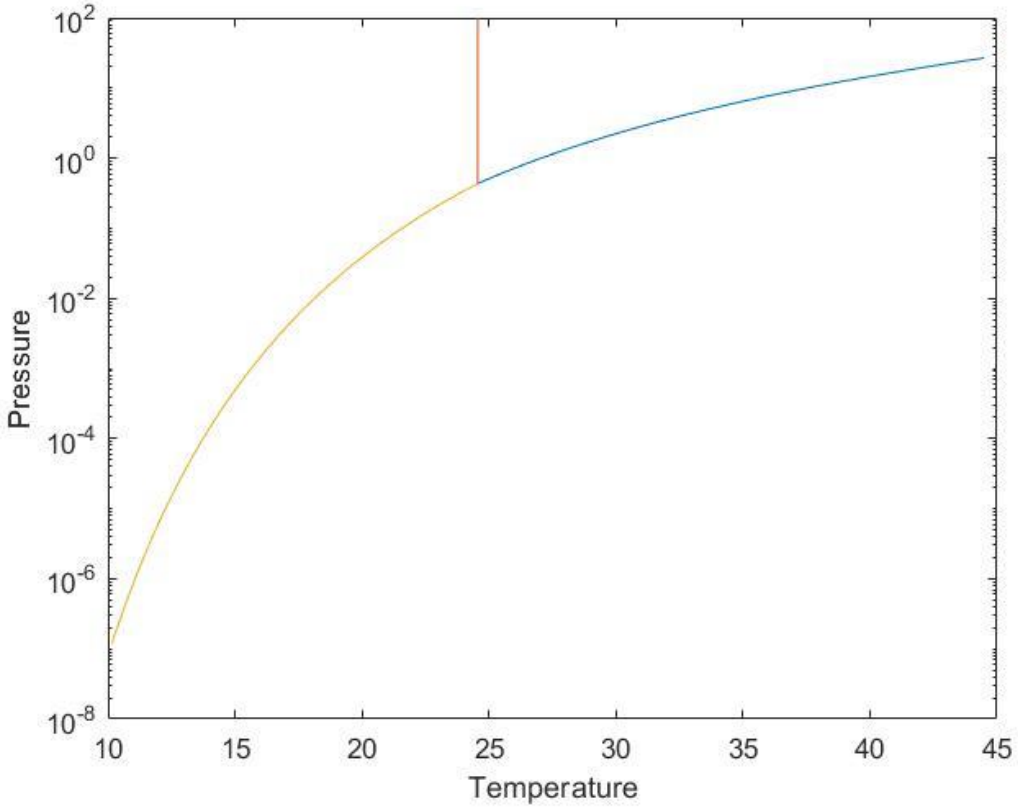

Figure 21: Phase diagram of neon.

Figure 20 is for nitrogen and we can see that there is limited data below 30K. Figure 21 is for neon and goes down to a temperature of 10 K. From the figures we can see that the choice of working fluid will have a large impact on whether or not condensation occurs.

3.2.3 Discrepancy With Results from Calculations

There are three different temperatures that need to be taken into account: 3 K, 10 K and 60 K as summarised in 2.3.3. The figures below clearly show that the 3 K and 10 K temperatures would imply that there would be condensation present. The data for Figure 22 and Figure 23 is also found from [24] and [25].

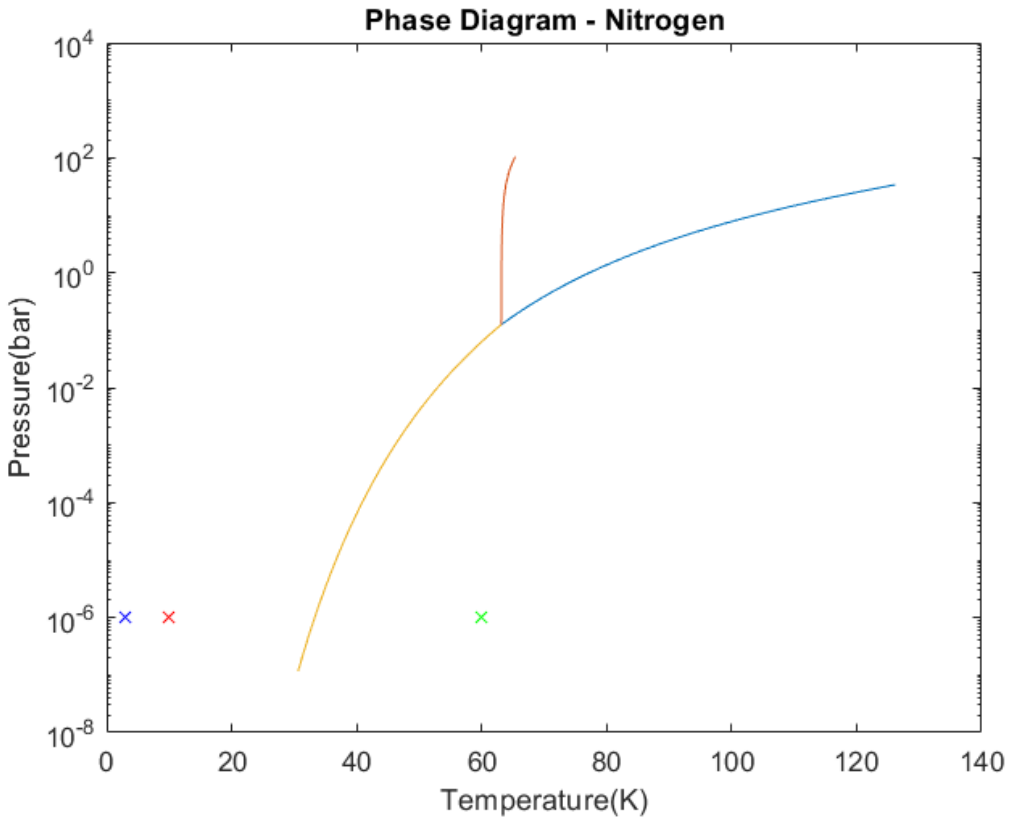

Figure 22: Phase diagram of nitrogen - blue cross 3 K, red cross 10 K, green cross 60 K.

In the case of Nitrogen only the 60 K result would imply that there is no condensation and the other temperatures would imply a change of state and therefore condensation.

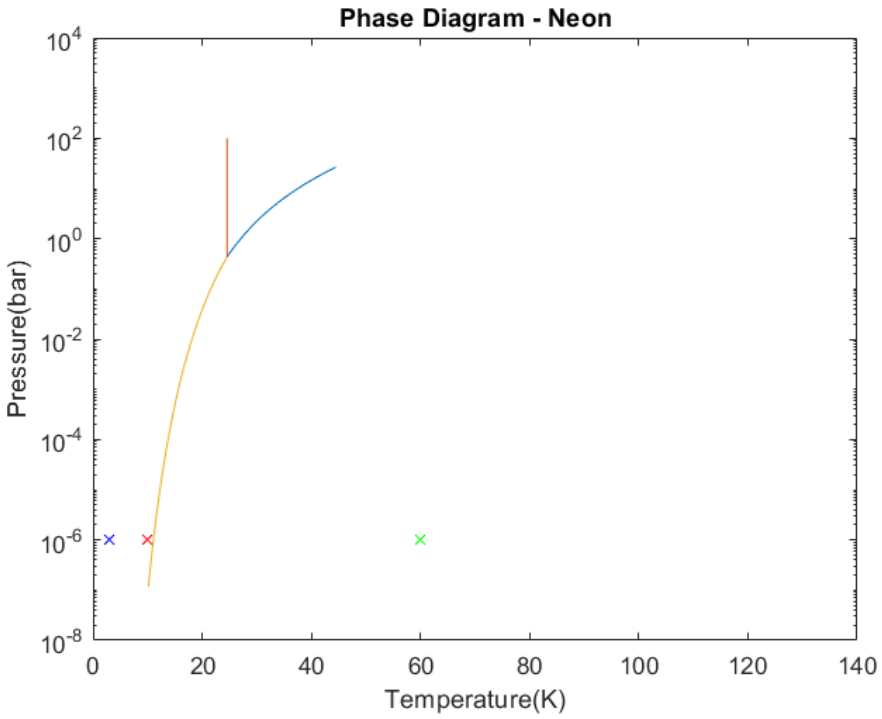

Figure 23: Phase diagram of neon - blue cross 3 K, red cross 10 K, green cross 60 K.

For neon, 60 K is still not an issue. The 10 K point is just next to the saturation line and therefore will unfortunately cause condensation to occur and the 3 K point is still too far and will cause condensation.

These results show that condensation will most likely still occur, but the results do not take into account the fact that this is a moving flow. The flow regime has a major influence on whether or not condensation occurs beyond the saturation line due to a process called supercooling.

3.2.4 Supercooling due to Super/Hypersonic Flow

Supercooling is a non-equilibrium effect that occurs when the flow expansion is fast enough. It means that flows can be at temperatures below their equilibrium saturation temperature and still not be condensed. The result of this is that the saturation line can effectively be shifted to the left and the extent of that is simply determined by expansion rate [26].

Supercooling could prove to be very useful since it allows the experiment to operate at a much lower temperature than originally calculated. In some cases, supercooling would allow the temperature to be shifted by as much as 20K. This means that the 10 K temperature that was found in the literature is much more acceptable and that 3 K is potentially viable.

This is exemplified by the following diagram:

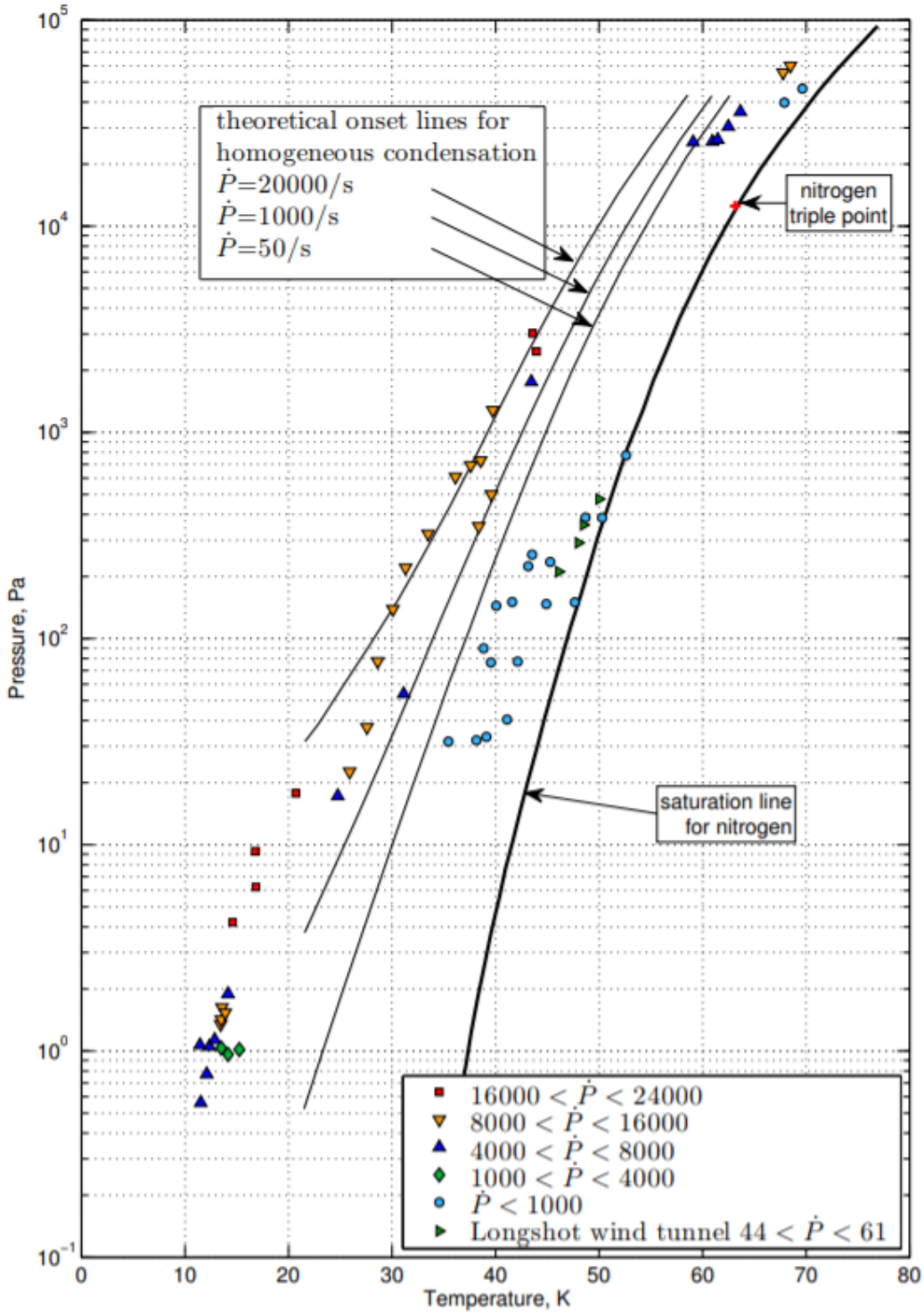

Figure 24: Phase diagram of nitrogen with data points representing first points of condensation from [26].

The diagram has the saturation line of nitrogen clearly shown. The different points that are present indicate the first occurrence of condensation measured. The different contours indicate the rough bounds of the shifted saturation line of the gas due to different expansion rates. With an increase in

expansion rate comes an increase in the amount of supercooling that is possible. The diagram clearly shows that as we move to lower temperatures the expansion rate increases.

The expansion rate is defined by:

$$\dot{P} = -\frac{dp/dt}{p} = -\frac{dp/dx}{pu} \quad \text{(Eqn. 8)}$$

This can be summarised as the rate of pressure decrease divided by the static pressure. This will be largely increased by having continuous flow nozzles such as conical and wedge nozzles. Any contoured nozzles will not have a large expansion rate. The converging-diverging nozzle that has been analysed is considered to be a conical nozzle and from calculations has got an expansion rate of 1.42×10^6. This value has been calculated from the values of pressure and velocity obtained from the ANSYS Fluent model.

If we were to plot the temperature of 10 K on the above diagram we can clearly see that it will be comfortably in line with the other plotted points, but it would have a much higher expansion rate and therefore a much higher degree of supercooling. From this observation we can see that for 10 K and 60 K with this type of nozzle there will be no condensation.

3 K is much harder to predict since there are no data points in the area and the lines of theoretical onset of condensation as shown in the figure do not stretch that far down. If the data for the highest expansion rates, the red squares, is extrapolated in a straight line it would intercept the pressure axis above the origin. This is clearly not possible as there cannot be any negative values on the Kelvin temperature scale. This implies that that the extrapolation needs to be curved and would need data points closer to the T=3 K.

3.3 Clusters

3.3.1 Basics of Clusters

Clusters are the initial form of droplets and comprise of a relatively small number of atoms held together by the Van der Waals force. They can be either homogeneous or heterogeneous depending

on whether there is another molecule present. There are empirical equations which can be used to estimate their size and even the average number in a given environment.

3.3.1.1 How Clusters are Formed

The first process is homogeneous nucleation which involves only molecules with the same atomic structure. Clusters will form due to Van der Waals forces and may also disintegrate randomly. This process of formation can be exacerbated by increasing the number of molecules present in the chamber. By increasing the number of molecules and therefore saturating the chamber a lot more collisions will occur. This means that the clusters can increase until they have achieved a critical size at which point, they are stable and will not disintegrate. This stability occurs when sum of Gibbs free energy for surface and volume have reached a maximum.

The other process is that of heterogeneous nucleation where a different molecule can aid the process of cluster formation. This other molecule does not need to be in a gaseous form to have an effect on the nucleation. This process has been ignored for this project since it is unlikely to occur due to the lengthy and thorough start-up procedures that are adopted at CERN.

3.3.1.2 Van der Waals Forces

This force happens to be one of the weakest intermolecular forces and relies on the forces present between electric charges. Electrons in molecules are thought of as a cloud which is usually uniform and therefore has a neutral distribution throughout. The motion of electrons is random and this means there will be times when there are more electrons present on one side of the cloud than another. This causes an instantaneous dipole where there is more of one type of charge than on the other, so where there are more electrons it is δ^- and the other end will be δ^+. Since electrons have random motion they could then move over to the other end of the molecule and then change the direction of instantaneous dipole.

If a molecule has got an instantaneous dipole and there is another molecule nearby the charge imbalance can cause a change in electron cloud of the second molecule, thereby inducing another dipole. If the electrons in the first molecule change position, then it will affect the electrons in the second molecule and both dipoles would have changed orientation.

This idea can then be expanded from two molecules to a much larger number, say 1000. All the directions of the induced dipoles will of course change in unison and the direction of the instantaneous dipole is changed. This the force which is partly responsible for the boiling points elements and molecules and it is one of the weakest intermolecular forces present [27].

3.3.1.3 Size

There is no clear-cut equation which estimates the size of a cluster, but research has been carried out to find a way of applying a scaling law to get a value. This method uses the Hagena parameter which is dependent on number density, nozzle density, initial temperature and some other constant values.

The equation for calculating the Hagena parameter is as follows:

$$\Gamma = n_0 d^q T_0^{0.25q-1.5} \quad \text{(Eqn. 9)}$$

Here n_0 is the number density of the molecule, increasing this value is similar to increasing the pressure. d is the diameter of the nozzle. T_0 is the initial temperature of the molecules. q is a scaling parameter used to ensure that the model is consistent, it is also derived experimentally which means that for this project there is no value for q for this specific case.

The parameter is useful, but specific to a gas species and therefore it would be useful to find reduced Hagena parameter, Γ^*. This value can then be used to determine which scaling law is required, but first some other parameters need to be calculated.

$$r_{ch} = (m/\rho)^{1/3} \quad \text{(Eqn. 10)}$$

$$T_{ch} = \Delta h_0^0 / k \quad \text{(Eqn. 11)}$$

In equation 10, m is atomic mass and ρ is the density of the solid. In equation 11, Δh_0^0 is the sublimation enthalpy per atom at 0K and k is the Boltzmann constant.

These two parameters are then used to calculate the reduced Hagena parameter:

$$\Gamma^* = {\Gamma}/{\Gamma^*} = \Gamma r_{ch}^{3-q} T_{ch}^{(1.5-0.25q)} \quad \text{(Eqn. 12)}$$

The results of this can then be used to determine whether clusters will occur or not. Since this project will not result in a physical experiment being built there will be no value for *q* since it must be derived experimentally. From the literature we know that if Γ^*<200 then there will be no clusters formed, if Γ^*>1000 then there will be clusters forming with a minimum size of 100 atoms per cluster. There are also scaling laws which state that for if Γ^*>1000 then $N_c \sim p_0^{2.35}$ where N_c is the number of atoms per cluster and if $10^4 < \Gamma^* < 10^6$ then $N_c \sim p_0^{1.8}$ [28]. Without an exact value for q we will be unable to determine the exact value for Γ^* and therefore cannot calculate the expected size of the clusters.

3.3.2 Effects of Pressure

From the looking at equations above we can see that there is a clear dependence on temperature. The number density of a substance and the pressure are related so a larger initial pressure means that there is a larger initial number density. When we apply this to the formula for the reduced Hagena parameter we can see that the higher the pressure the higher larger the value of if Γ^*. This would mean that we are more likely to have larger clusters. Also the scaling law is proportional to the initial pressure so the larger the initial pressure the larger the particles will be. This result makes sense when we consider a phase diagram because as we increase the pressure from a gas, we will condense to form either a solid or gas.

3.3.3 Effects of Temperature

The reduced Hagena parameter is clearly inversely proportional to the initial temperature. As the temperature increases, if Γ^*decreases. This is completely in line with the understanding from phase diagrams as the temperature increases the substance goes further into the gaseous region.

4 MOLECULAR FLOW GAS JET MODELLING AND ANALYSIS

4.1 Background and Justification

In the region after the first skimmer, viscous flow effects cease to apply (section 2.3.3, and [29]) as the particle density and pressure is very low and the mean free path of molecules is larger than the gas apparatus (Knudsen number – section 2.1.4) [30] – effectively no collisions between molecules occur. Individual particles move in straight lines, and only collide with chamber walls. A “molecular flow” model for this region was identified as a useful tool for:

1. Informing/confirming the optimal flow parameters for the viscous flow side that would give good gas curtain performance. The gas curtain is effectively the “end goal” for this project to optimise, so it is essential for all work to be able to be linked to gas curtain performance.
2. Carrying out analysis of skimmer locations and geometries to optimise the end gas curtain.
3. Modelling aspects of the gas jet that would influence the design of the optical state measurement instrument (section 5) e.g. expected density ranges and laser gas jet heating.

Whether molecular flow theory applies depends on a number of factors (including density, pressure, and the geometry of the surroundings), and is usually determined by calculating the Knudsen number (section 2.1.4). Our calculations and information in prior literature on the gas apparatus confirm that molecular flow applies in the gas apparatus for the flow after the first skimmer.

Clusters of molecules may also form in the first chamber – depending on when these disintegrate, they may cause density spikes in the gas curtain which would interfere with profile measurements.

4.2 Model Design

Requirements for the Gas Jet/Curtain Model were discussed and agreed at the 25/02/2019 meeting.

R4.1 (Core): Input the nozzle output density, velocity & temperature data from the viscous flow model (section 2.3.2) to assign properties to a set number of “particles”.

R4.2 (Core): Simulate the trajectory of “particles” through the low-pressure gas apparatus, accounting for the geometry of the skimmers (with a kinematic/geometric approach).

R4.3 (Core): Be capable of simulating the behaviour of a system with a very large number of particles in a reasonable time. Ideally >10^6 particles in <5 minutes per simulation run.

R4.4 (Core): Allow the effects of added thermal energy (from laser light heating or nozzle heating) to be simulated in order to study the effects on the gas jet.

R4.5 (Extension): Allow the trajectory and behaviour of particle clusters to be simulated at a basic level, to investigate their impact on the gas curtain density.

The Molflow [31] simulation package (developed by CERN) was also considered as an alternative to building a model from scratch, but research showed that Molflow was not the correct tool for this project: Molflow is designed to run using input geometry from CAD programs, which would make it difficult to automatically run simulations with a range of computer-generated geometries. It also has no provision for the laser light heating or cluster analysis that were identified as key requirements. Lastly, the additional utility to CERN is limited as they already have Molflow results on the apparatus.

4.3 Model Implementation

A “Monte Carlo” model was implemented in MATLAB, and proved capable of running a large (>10^7 particles) simulation in less than 1 minute on a consumer PC. The probability distributions for particle velocities and positions are derived below, including some B14 techniques.

The mechanism which causes the gas jet to diverge over time, with increasing FWHM (Full Width Half Maximum - the width of the gas jet measured between the two points where its density falls to half its central peak density), is thermal motion in the radial direction. Molecular velocity also affects the resolution in the gas curtain: higher particle velocities will lead to larger displacements during the photon emission time, meaning that the gas curtain CCD will not receive a photon from exactly where the particle collision took place.

Before the first skimmer, viscous effects apply and there are enough collisions per second for the Maxwell-Boltzmann distribution to be used. Particles will therefore have their velocities assigned at the start of the simulation, accounting for the input thermodynamic temperature. As well as assuming molecular flow, the two major simplifying assumptions are explained below.

Assumption 1: Only velocity in the radial direction needs to be considered for thermal motion gas jet spreading – thermal velocity in the flow axis can be ignored. Firstly, the random thermal velocity in the flow axis is small relative to the bulk velocity in that direction - the bulk velocity is ~800 $m.s^{-1}$ [32], and the mean thermal random velocity is <100 $m.s^{-1}$ (section 4.3.4), only some of which will be in the direction of flow. Also, the velocity distribution in the direction of flow will be symmetrical about v=0, so across all molecules simulated the flow in either direction in the flow axis should cancel out.

Assumption 2: The gas jet model is rotationally invariant - expansion will be isotropic as thermal velocity is randomly distributed in all directions. This simplifies the model by exploiting symmetry - and the first two skimmers have circular apertures, so the radial position determines if they pass.

4.3.1 Overall Summary of Approach

1. Generate a large number of particles at the first skimmer from position and velocity statistical distributions derived below, with parameters informed by the output of the viscous flow model. The bulk radial velocity (dependent on radial position) is also added (figure 16).
2. Calculate the trajectory of each particle, accounting for the bulk velocity v_x.
3. At each skimmer, skim particles off based on a kinematic model using their radial position, radial velocity and the geometry of the skimmer.
4. Continue the simulation to the point where the gas jet interacts with the particle beam.

4.3.2 Gas Jet/Curtain Model Coordinate Systems

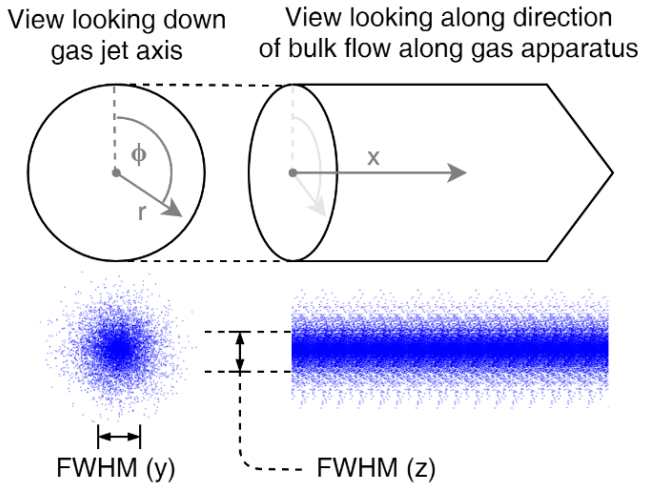

Figure 25: Coordinate frame/FWHM example.

- r (position) and v_r (velocity) are in the radial direction. ϕ is the polar angle.
- x (position) *and* v_x (velocity) are in the direction of flow along the gas apparatus.
- The origin (x=0) is the centre of the aperture of the first skimmer.
- The coordinate system applies to the model and derivation in section 4.3.

4.3.3 Particle Radial Velocity Distribution Derivation from Maxwell-Boltzmann

The Maxwell-Boltzmann velocity probability distribution in spherical polar coordinates [33] is:

$$f(v,\theta,\Phi) = (\frac{m}{2\pi kT})^{1.5} v^2 \exp\left(-\frac{m}{2kT}v^2\right)\sin\theta \qquad 0 \le \Phi < 2\pi, 0 \le \theta < \pi, 0 \le v < \infty \qquad \text{[33]} \quad \text{(Eqn. 13)}$$

We then marginalise Φ as the model should be Φ-invariant (assumption 2 in section 4.2):

$$f(v,\theta) = \int_0^{2\pi} f(v,\theta,\Phi)\mathrm{d}\Phi \; = 2\pi(\frac{m}{2\pi kT})^{1.5} v^2 \exp\left(-\frac{m}{2kT}v^2\right)\sin\theta \qquad 0 \le \theta < \pi, 0 \le v < \infty \quad \text{(Eqn. 14)}$$

To find the radial velocity distribution, it is simpler to marginalise x-axis velocity in Cartesian coordinates $f(v_\mathrm{r}, v_\mathrm{x})$ rather than calculating velocity components in polar coordinates $f(v,\theta)$.

$$f(v_\mathrm{r}, v_\mathrm{x}) = f(v,\theta)\left|\frac{\partial(v,\theta)}{\partial(v_\mathrm{r},v_\mathrm{x})}\right| \qquad \left|\frac{\partial(v,\theta)}{\partial(v_\mathrm{r},v_\mathrm{x})}\right| = \frac{1}{|v|} = \frac{1}{|{v_\mathrm{r}}^2 + {v_\mathrm{x}}^2|} \qquad v = \sqrt{{v_\mathrm{r}}^2 + {v_\mathrm{x}}^2}, \theta = \tan^{-1}\left(\frac{v_x}{v_r}\right)$$

$$f(v_\mathrm{r}, v_\mathrm{x}) = 2\pi(\frac{m}{2\pi kT})^{1.5}({v_\mathrm{r}}^2 + {v_\mathrm{x}}^2)\exp(-\frac{m}{2kT}[{v_r}^2 + {v_x}^2])\sin(\tan^{-1}\left(\frac{v_\mathrm{x}}{v_\mathrm{r}}\right))\frac{1}{|{v_\mathrm{r}}^2 + {v_\mathrm{x}}^2|} \qquad \text{(Eqn. 15)}$$

$$\sin(\tan^{-1}\left(\frac{v_\mathrm{x}}{v_\mathrm{r}}\right)) = \frac{v_\mathrm{x}}{v_\mathrm{r}\sqrt{\frac{{v_\mathrm{r}}^2 + {v_\mathrm{x}}^2}{{v_\mathrm{r}}^2}}} = \frac{v_\mathrm{x}}{\sqrt{{v_\mathrm{r}}^2 + {v_\mathrm{x}}^2}}$$ (technically $\pm$, but probability distribution must be positive).

$$f(v_\mathrm{r}, v_\mathrm{x}) = 2\pi(\frac{m}{2\pi kT})^{1.5} v_\mathrm{x} \exp(-\frac{m}{2kT}[{v_\mathrm{r}}^2 + {v_\mathrm{x}}^2]) \qquad \text{(Eqn. 16)}$$

To find the distribution for v_r, v_x is marginalised between 0 and infinity (v_x is only a magnitude value as the negative direction has already been marginalised):

$$\int_0^\infty 2\pi(\frac{m}{2\pi kT})^{1.5} v_\mathrm{x} \exp(-\frac{m}{2kT}[{v_\mathrm{r}}^2 + {v_\mathrm{x}}^2])\,\mathrm{d}v_\mathrm{x} \qquad = f(v_\mathrm{r}) = \sqrt{\frac{m}{2\pi kT}}\exp(-\frac{m}{2kT}{v_\mathrm{r}}^2) \qquad \text{(Eqn. 17)}$$

Equation 17 is clearly a Gaussian (normal) distribution with variance $\frac{kT}{m}$: $f(v_\mathrm{r}) \sim \mathrm{N}(v_\mathrm{r}; 0, \frac{kT}{m})$.

The result has the expected properties of zero mean and symmetrical distribution, and can also be verified by calculating the RMS velocity magnitude in both the original and the derived distributions.

4.3.4 Verifying Derived Velocity Distribution

N_2 molar mass is given in table 2. *R* is the universal gas constant, *T* is thermodynamic temperature.

From the radial velocity distribution (equation 17): standard deviation $\sigma = \sqrt{\frac{kT}{m}} = \sqrt{\frac{RT}{M}}$. The mean absolute value of a zero-mean normal distribution is equal to: $v_{\mathrm{r,mean\,abs}} = \sigma\sqrt{\frac{2}{\pi}} = 43.47\ \mathrm{m.s^{-1}}$.

Average molecular velocities (in all directions) according to the standard 3D Maxwell-Boltzmann velocity distribution [34] are: (taking the gas jet temperature as 10 K from reference [32]):

RMS: $v_\mathrm{RMS} = \sqrt{\frac{3RT}{M}} = 94.365\ \mathrm{m.s^{-1}}$ [35]. Mean absolute: $v_\mathrm{mean} = \sqrt{\frac{8RT}{\pi M}} = 86.940\ \mathrm{m.s^{-1}}$ [35].

It is simpler to consider a hemisphere to compare mean velocities: we are considering the mean of absolute velocity for the derived distribution (as the mean velocity would simply equal zero), so the negative direction is ignored. From [12] p.33: the centre of mass of a thin hemispherical shell is $\bar{y} = \frac{r}{2}$. This is equivalent to stating that the average component in a single axis (e.g. *y*) of a vector of size *r* that is equally distributed in all forward directions (i.e. vectors pointing to every point on a hemispherical shell of radius *r*) is equal to $\frac{r}{2}$. Therefore, one would expect the mean absolute velocity in the radial direction to be equal to half of the mean velocity in all directions. From above, $v_{\mathrm{r,mean\,abs}} = v_{\mathrm{mean}} \,/\, 2$. In summary, the derived distribution has all of the expected properties.

4.3.5 Particle Position Distribution

The input from the viscous flow model (section 2.3.2) showed that the particle density at the first skimmer was constant across the aperture. However, simply drawing radial positions from a uniform distribution would cluster most particles around the centre of the aperture. The Jacobian area element for 2D polar coordinates $\mathrm{d}A = r\ \mathrm{dr}\ \mathrm{d}\theta$. Therefore, for an even density distribution across the aperture, the particle positions should be drawn from a triangular distribution as illustrated in the first graph of figure 26 – the position probability distribution $\mathrm{p}(r) \propto |r|$.

4.4 Results

The simulation focus was on the areas of interest defined in section 4.1. “Default” dimensions for the simulated gas apparatus (for when graphs are produced varying one geometric factor, leaving others constant) were based on information about the Cockcroft prototype apparatus, sourced from discussion with Hao Zhang at the Cockcroft Institute as well as figures/values in several of the papers published by the Cockcroft research group - [7] [36]. The “default” input temperature for gas through the first skimmer was taken as 10 K, which was the value given in almost all literature. Molecular nitrogen was used as the working gas species for these simulations.

Similar trends in the results would be seen if neon was used as the working gas, but numerical values would differ because the atomic mass of Ne (20.18 u - [37]) is smaller than the molecular mass of N_2 (28.01 u - [37]). Therefore, Ne atoms would have a higher average radial thermal velocity.

4.4.1 Single Simulation Run Analysis

The model was validated at a basic level by comparing the outputs of this simulation run (set up with Cockcroft prototype gas apparatus dimensions) with results from literature based on the same apparatus. This gave a good degree of agreement, particularly for the proportion of gas that passes through to the gas curtain [36].

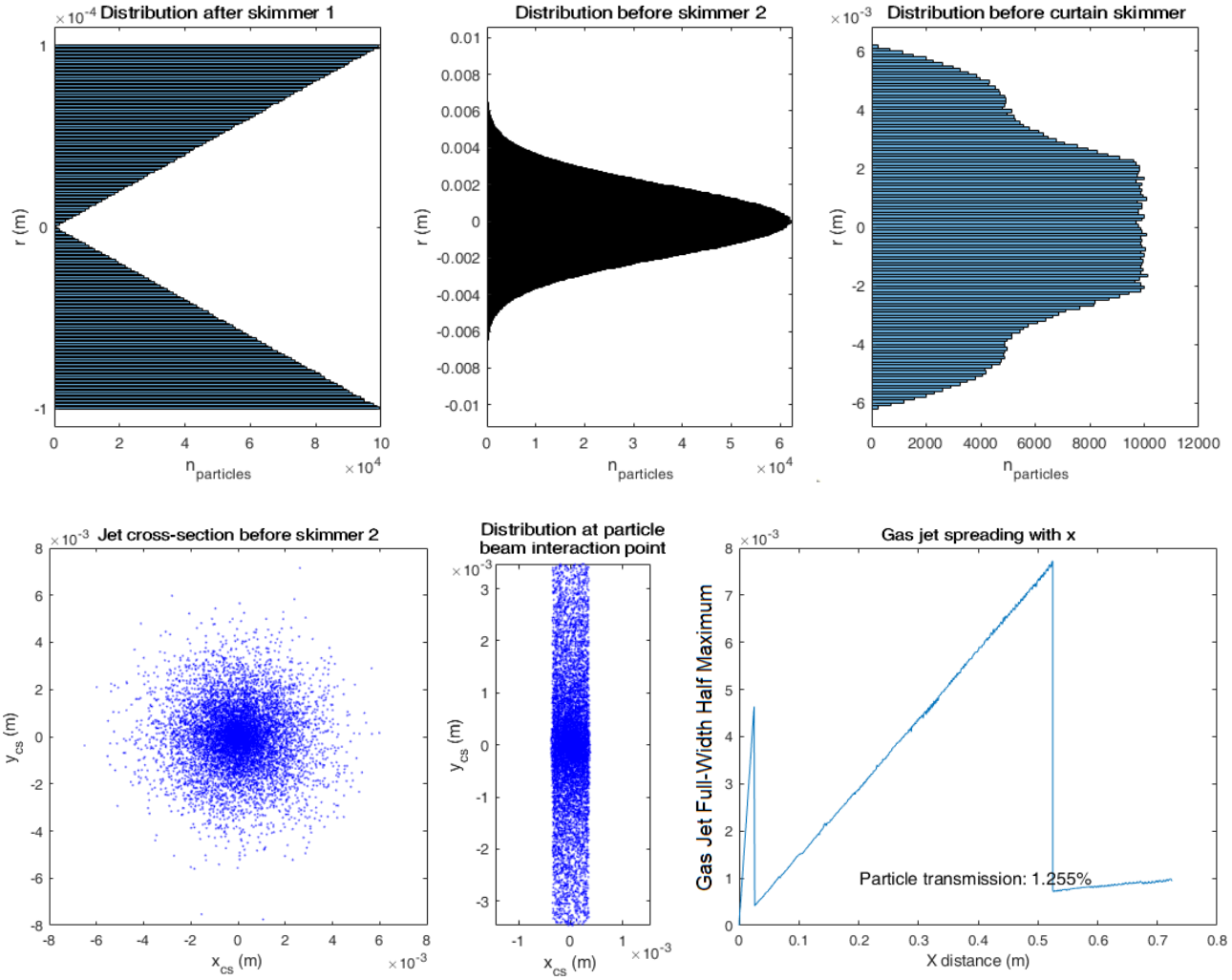

Figure 26: Illustrative graphs for a single simulation run. The top three (radial distribution) and bottom left 2 figures (cross section) show the distribution at different points in the gas jet, and the bottom right is a graph of FWHM throughout the gas jet, with the particle transmission percentage.

In figure 26 it can be seen that the gas rapidly forms into a roughly normal radial distribution (top centre graph) in the short 25mm distance between skimmer 1 and skimmer 2, due to the range of thermal velocities. After the outer part of this distribution is skimmed off by skimmer 2, and the gas jet undergoes further thermal expansion, the distribution appears as in the top RHS graph – the “flat edge” on the distribution is a similar width to the long dimension of the curtain skimmer. This suggests that the centre of the gas jet flow (and therefore the gas curtain) will have the highest molecular

density, as is also illustrated in figure 27. The bottom right graph of figure 26 shows the collimating action of the skimmers on FWHM. This simulation gave a result of 1.255% of gas molecules that make it through skimmer 1 reaching the gas curtain without being skimmed off and evacuated.

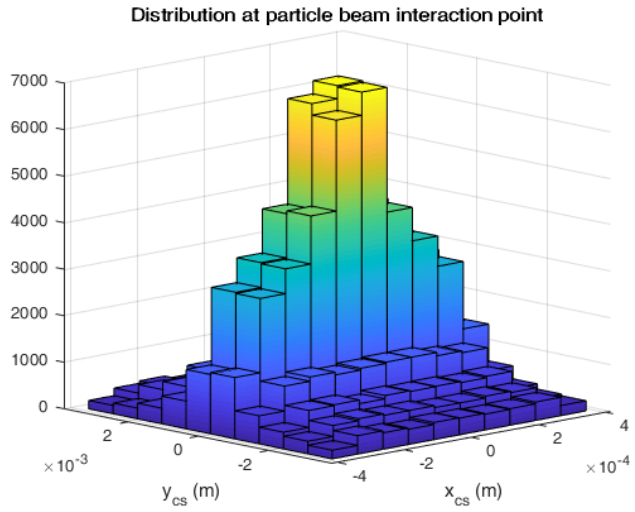

Figure 27: 2D density distribution at gas curtain / particle beam interaction point.

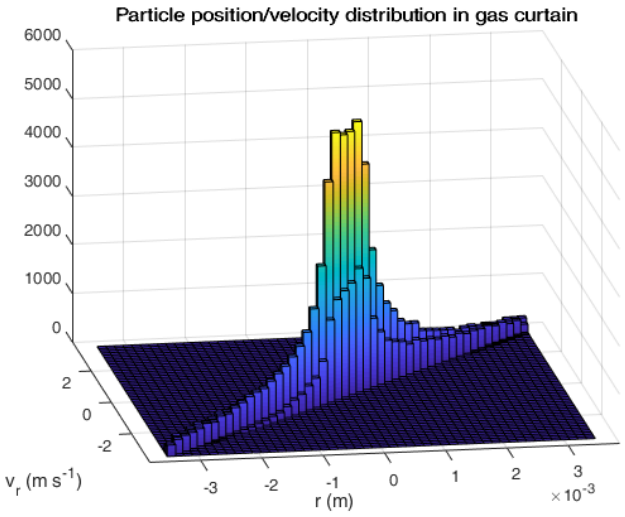

Figure 28: Strong correlation between radial position and radial velocity.

Figure 28 shows that in the gas curtain there is a strong positive correlation (correlation coefficient ≈ 0.95) between a molecule's radial position and its radial velocity. A velocity prediction can be used to decrease profile measurement uncertainty by extrapolating backwards from where a photon was emitted, using the average decay time for photon emission. Extrapolation is also important for the bulk flow direction, where the bulk velocity is both high and broadly constant across all molecules.

4.4.2 Effects of Changing Input Temperature (Multiple Simulation Runs)

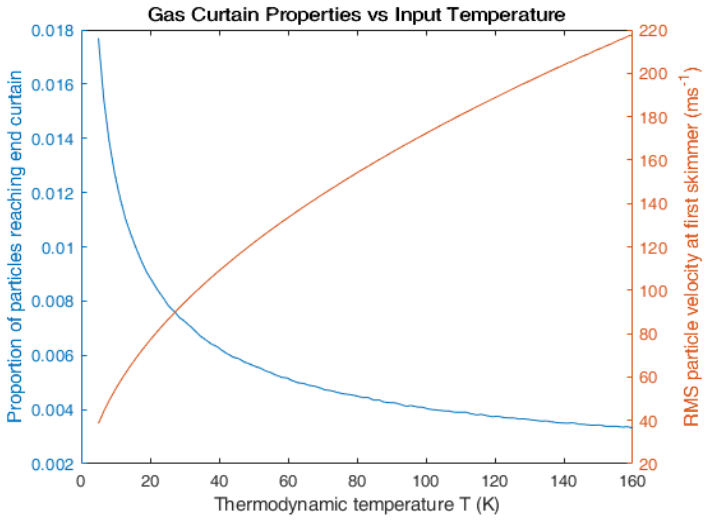

Figure 29: Gas input temperature effects.

The blue plot of figure 29 shows the inverse relationship between the temperature of the gas passing through the first skimmer and the proportion of gas that reaches the gas curtain (pass proportion). The cause for this is shown by the red plot on the graph: this shows how the RMS molecular radial velocity at the first skimmer (the model input) increases with temperature as $\propto \sqrt{T_{\text{in}}}$. However, the RMS velocity of molecules that do reach the

gas curtain remains unchanged. Overall, as the density of the gas curtain is a design factor to be maximised, this confirms that a design goal on the viscous flow side should be to minimise gas temperature at the first skimmer.

4.4.3 Gas Apparatus Geometry Effects

For the Gas Jet/Curtain Model, skimmer dimensions and geometry are as defined as in figure 4. The (internal) skimmer angle determines the range of particle velocities that will be allowed through the skimmer, for particles that are close to the skimmer edge. Displacements/locations are measured from x=0 at the centre of the first skimmer.

4.4.3.1 Curtain Skimmer Geometry and Location

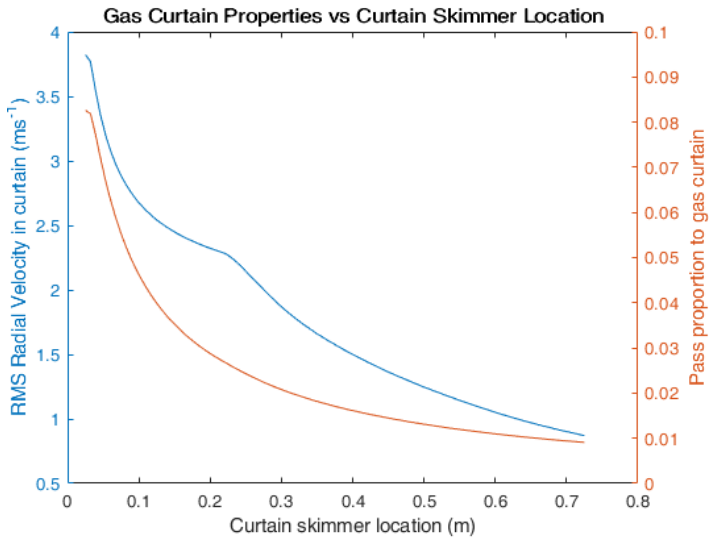

Figure 30: Curtain skimmer location effects on pass proportion and average molecular velocity.

Figure 30 suggests that (for a rectangular skimmer) it is desirable to have a curtain skimmer location of <0.1 m or >0.6 m, in order to maximise the pass proportion (red, design factor to ideally maximise to increase gas curtain density) compared to the RMS radial velocity of molecules in the gas curtain (blue, design factor to ideally minimise to reduce measurement error in the gas curtain as detailed in section 4.4.1). The RMS radial velocity plot (LHS) does show the expected monotonic decreasing behaviour, with the slight "bump" near x=0.25 being an artefact of the aspect ratio of the curtain skimmer. Therefore, ideal curtain skimmer location will be heavily influenced by its aspect ratio.

The gas curtain properties are effectively completely defined by the curtain skimmer, not the other two skimmers, as the curtain skimmer effectively sets the end solid angle that molecules have to pass through to reach the gas curtain.

The internal angle of the curtain skimmer does not appear to have a significant effect on the curtain from a geometry / solid angle point of view. A small skimmer angle skimmed off fewer particles near

the edge than an equivalent skimmer with a large skimmer angle, but this effect was largely negligible for this skimmer (due to the relatively large aperture size), and changing skimmer angle functionally had the same effect as simply increasing aperture size or moving the curtain skimmer closer to the first skimmer to increase solid angle that way. Skimmer angle also is also a much more important consideration when viscous flow equations are still in effect [38] i.e. nearer the gas apparatus nozzle.

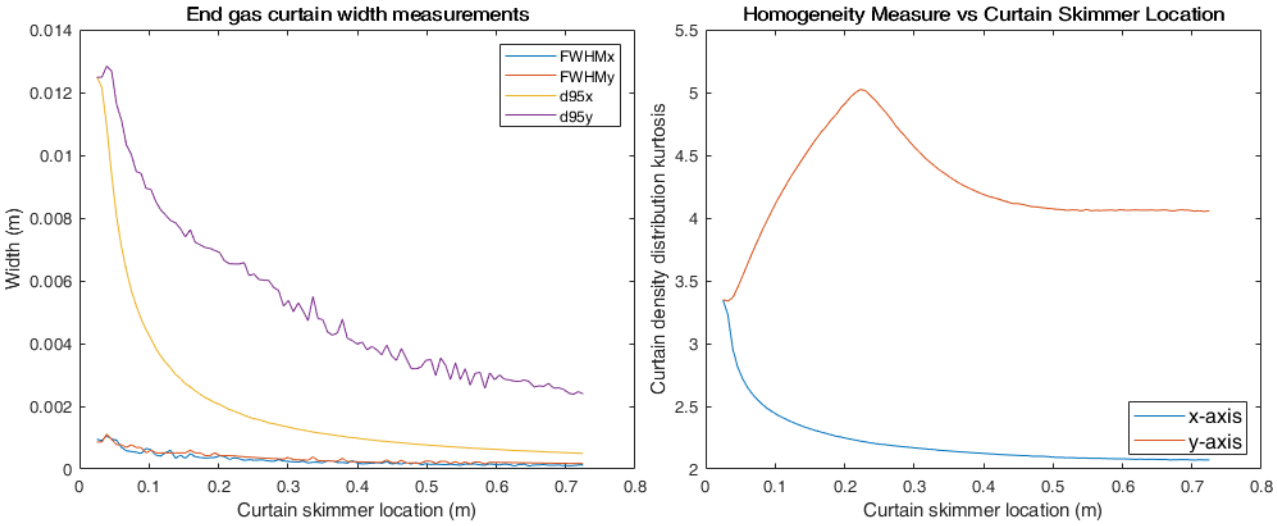

Figure 31: Effect of curtain skimmer location on gas curtain homogeneity and width.

Figure 31 illustrates another important consideration for the curtain skimmer location: density homogeneity of the gas curtain at the interaction point with the particle beam. The probability of photon emission from a point in the gas curtain is directly proportional to the gas density at that point – therefore, any density variation will interfere with the beam profile measurement.

These graphs use cross-section coordinates for gas curtain: the x axis measures the “thickness” of the gas curtain, and the y axis measures the “width” of the gas curtain. The LHS graph of figure 31 shows two ways of measuring width in x and y dimension – the Full Width Half Maximum (FWHMx and FWHMy) and the 95% full width (similar to FWHM, but measuring the point at which the density drops to 5% of the maximum density). The figure shows that the FWHM measures for x and y are very similar – i.e. gas molecules are still concentrated around the centre of the curtain cross section. Homogeneity is also measured with sample kurtosis in the RHS graph – lower kurtosis would suggest a better density homogeneity. This suggests that density homogeneity in the curtain is better through its cross-sectional thickness than across its width. Density homogeneity is however less important for the curtain thickness, which should be minimised to reduce camera parallax error.

Overall, density homogeneity is not generally very high across the width of the gas curtain – rather than being an ideal, “rectangular” cross section, the density distribution has a significant peak at the centre. However, as the particle beam diameter is very small, the centre of the gas curtain should be homogenous enough in the region the gas curtain interacts with the particle beam.

4.4.3.2 Skimmer 2 Geometry and Location

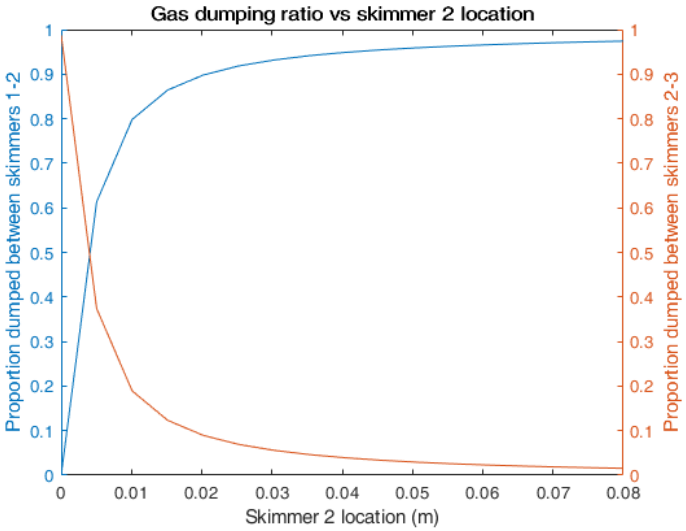

Figure 32: Effect of skimmer 2 location on ratio of gas molecules removed from each chamber.

As with the curtain skimmer, the action of the skimmer is defined by the solid angle of its aperture from the point of view of the origin, so for this section the skimmer dimensions are fixed and the distance between the first two skimmers is varied.

As section 4.4.3.1 shows, the gas curtain is effectively just defined by the curtain skimmer, and skimmer 2 effectively has no influence. The effect of the skimmer 2 placement is to adjust the proportion of molecules that are skimmed off and removed in each chamber. Ensuring that a much larger proportion (~10x) of molecules are skimmed off in the first chamber (between the first/second skimmers) than the second chamber (between the second/curtain skimmers) allows the pressure to be dropped chamber by chamber from the high pressure in the nozzle chamber to the near-vacuum pressure at the beamline.

4.4.4 Gas Jet Heating via Laser Light

If laser light is incident on the gas jet, gas molecules may absorb/re-emit photons that have a wavelength close to an absorption peak for that gas species – this may cause a temperature increase as the photons transfer momentum. Hand calculations using equations from [39] showed that even in the worst case of fully spontaneous emission after a laser photon is absorbed by the gas, and all photon momentum adding up in the same direction, the amount of thermal energy imparted to the gas jet is negligible for all reasonable laser powers (<100 W). Molecules are not in the laser beam long enough for their temperature to increase more than about ~0.5% in the absolute worst case.

5 Optical Gas Jet Characterisation System Design

5.1 Background and Justification

Previous sections have established that the ideal gas jet for gas curtain formation should have a number of key attributes: high density (and homogeneity), high velocity, low temperature, etc.

Much of the current gas apparatus design is built on data from computational models of the gas jet flow – in general, ANSYS Fluent for the high-pressure nozzle side and Molflow [31] for the molecular flow gas jet. Two computational approaches are covered in this report in sections 2.3.2 and 4. However, the computer modelling approaches (especially on the viscous side) have severe issues managing the greatly differing pressure and length scales, which vary by many orders of magnitude. (30 μm nozzle diameter → ~300 mm distance to 2nd skimmer, and pressure ranges from ~5 bar to ~5x10^{-6} bar in the first chamber alone). This was an issue that was brought up several times by CERN, researchers at the Cockcroft Institute and Oxford 3YP team members during the project – the computational models are not very reliable and often do not converge. To add to this problem, there is little prior research into gas supersonic expansion into a vacuum. There is currently some ability to measure gas pressure in the Cockcroft prototype apparatus with a vacuum gauge, but this is invasive (it disturbs the measured flow), and is very limited in resolution and where it can measure.

A non-invasive, high resolution/accuracy and flexible experimental instrument would be highly useful to validate the computational models that much of the gas apparatus design is based on, confirm that the gas jet is behaving as expected and potentially lead to new gas apparatus design insights.

5.2 Comparison of Methods

Background research was carried out to compare different possible measurement approaches. An optical measurement approach was quickly identified as a much more suitable option than physical invasive measurements (e.g. movable pitot probe) for ensuring that the instrument does not affect the gas jet being measured. Three candidate optical techniques that are often used for non-invasive measurement [40] were compared in the multi-factor analysis in table 7 – for this analysis, approaches are scored on several criteria from 1 (least suitable) to 5 (most suitable). Some

approaches were considered but were not useful to analyse via a multi-factor analysis (e.g. Particle Image Velocimetry, which requires the flow to be seeded with relatively large particles, is definitely unsuitable). The complex theory behind each approach will not be given in any significant depth, as this analysis is only for comparison between approaches.

Criteria	Weight	**Raman Scattering** – inelastic photon-molecule scattering		**Rayleigh Scattering** – elastic scattering		**Laser Doppler Velocimetry**	
		Rating	Score	Rating	Score	Rating	Score
Effective cross-section	**4**	**1** – very weak process.	**4**	**3** – relatively weak scattering.	**12**	**4** – but performs better with seed particles.	**16**
Ability to measure required states	**5**	**4** – capable of measuring all required states.	**20**	**5** – measures all required states simultaneously.	**25**	**4** – capable of measuring all required states.	**20**
Optical complexity	**3**	**4** – simple setup, one laser required.	**12**	**4** – simple setup, one Laser required.	**12**	**1** – complex, 2 coherent sources needed + tuning.	**3**
Potential signal interference	**3**	**2** – Rayleigh photons will interfere.	**6**	**2** – large particles may interfere.	**6**	**3** – no obvious large sources of interference.	**9**
Total			**42**		**55**		**48**
Notes and common applications		Can determine the composition of gas mixtures– useful for combustion analysis.		Cannot differentiate between gas species – but this is not an issue for our application.		Very popular for use in fluid flow analysis – but cannot differentiate gas species.	

Table 7: Multi-Factor Analysis of common optical flow measurement approaches.

Effective cross-section (effectively a measure of probability of the process occurring for each molecule) for the optical process is highly important as this is directly proportional to the number of photons received when performing the measurements. It is very important to receive as many photons as possible to reduce measurement uncertainty, as covered in section 5.5. Of all options considered, an optical instrument based on Rayleigh scattering was shown to give the best combination of capabilities, setup complexity and estimated measurement time.

5.3 Requirements Definition

NASA literature detailing previous experiments with Rayleigh scattering diagnostics [41], hand calculations (including sensible estimations) with equations in section 5.5 using Cockcroft prototype

gas apparatus dimensions (section 4.4), and knowledge of the key areas of interest for measurement were used to define an achievable, focused set of requirements for the instrument.

R5.1: The instrument shall be capable of measuring gas bulk velocity in the direction of flow with an uncertainty of ±5% (equivalent to ±40 $m.s^{-1}$ at bulk velocity of 800 $m.s^{-1}$), and be capable of measuring bulk velocity in the range 400 $m.s^{-1}$ to 1200 $m.s^{-1}$.

R5.2: The instrument shall be capable of measuring gas density with an uncertainty of ±5%, in the gas density range $1.5x10^{-9}$ $kg.m^{-3} < \rho < 1x10^{-6}$ $kg.m^{-3}$, to be able to be used feasibly to measure any point of interest in the gas jet (density figures based on gas curtain density given in [7], extrapolated backwards by the pass proportion calculated in section 4.4.1).

R5.3: The instrument shall be capable of measuring gas temperature with an uncertainty of ±5K.

R5.4: The instrument shall be capable of quantifying the presence of cluster/droplets in the jet.

R5.5: The instrument shall have a measurement time (which may depend on resolution) which is low enough to make the instrument practical (e.g. not 24 hours per measurement).

R5.6: The instrument shall have a volumetric measurement resolution of at most 1 mm^3, and should ideally be capable of a more precise volume resolution of e.g. $(0.1\ mm)^3$.

R5.7: The instrument should be designed for minimal invasiveness, so it does not affect the gas jet being measured (e.g. should not require seeding the gas flow with reflective particles).

R5.8: The instrument should ideally be capable of working with both N_2 and Ne as the gas species used, and should be feasible to be integrated with the prototype gas apparatus.

5.4 Underlying Physical Principles and Analysis of Scattering Types

The principles underlying the approach are illustrated in figure 33. Photons with a narrow frequency range are produced by a coherent laser source - these are focused onto the measurement volume inside the gas apparatus. A small proportion of the photons are scattered from molecules/clusters in the volume via elastic scattering (the two types of scattering occurring are discussed below). The frequency of each photon will be doppler shifted depending on the velocity component (in the scattering direction) of the particle being scattered from. Scattered photons that pass through the solid angle of the receiver are analysed to give readings for the states of interest.

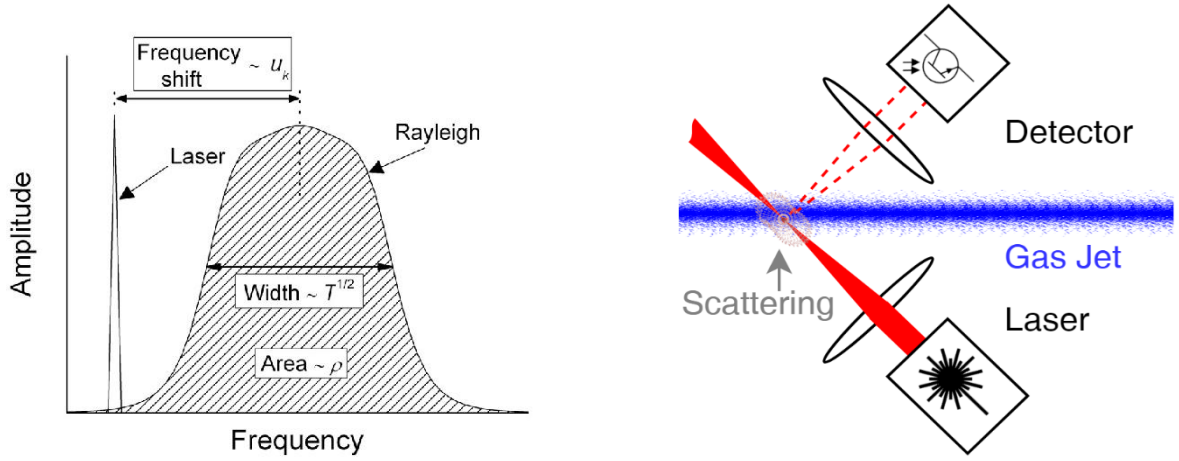

Figure 33: LHS: Illustration of state measurements from doppler shift of photon scattering [41]. The RHS diagram shows the experimental layout with a 90° scattering angle.

1. u_k (component of bulk velocity in the scattering direction) is found from the doppler shift between the laser frequency and the maximum of the scattered light frequency distribution.
2. The width of the scattered light frequency distribution gives the range of particle velocities, which can then be used to find the bulk temperature ***T*** via the Maxwell-Boltzmann distribution.
3. The density of the gas at the measurement point ***ρ*** is directly proportional to the number of photons received, as elastic scattering is a purely linear process.

5.4.1 Rayleigh Scattering – Individual Molecules and Small Clusters

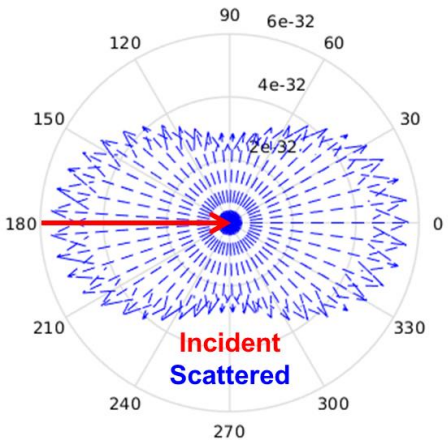

Figure 34: Rayleigh angular scattering intensity distribution (in plane of light polarization).

Rayleigh scattering applies when the size of the scattering particle is far smaller than the incident light wavelength ($d \ll \lambda$). The angular intensity distribution of Rayleigh scattered energy from a single molecule is given by equation 18.

$$\frac{I}{I_0} = \frac{8\pi^4 N\alpha^2}{\lambda^4 R^2}(1+\cos^2\theta) \qquad [42] \qquad \text{(Eqn. 18)}$$

α is molecular electrical polarizability, N is the number density and R is radius from the molecule.

The angular scattering distribution from a single molecule of N_2 is shown in figure 34. Power is radiated roughly equally in all directions. Importantly, from equation 18, the scattering has a strong dependence on light wavelength – shorter wavelengths are scattered far more than longer wavelengths. This is the mechanism that makes the sky appear blue.

5.4.2 Mie Scattering – Large Clusters

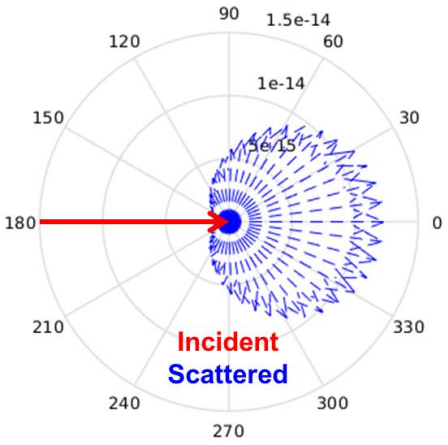

Figure 35: A Mie scattering angular intensity distribution (in plane of light polarization).

Mie scattering applies when the size of the scattering particle has a similar length scale to the incident light wavelength ($d \approx \lambda$). The angular scattering distribution is highly dependent on particle size, but in general more power is radiated in the forward direction. An analytic solution is not available, and the distribution must be found by computationally intensive numerical approaches which involve solutions to Maxwell's equations in free space.

The angular scattering distribution for a large cluster of N_2 molecules is shown in figure 35. Mie scattering has much less of a wavelength dependence than Rayleigh scattering, but can scatter significantly more intensity - especially in the forward direction.

5.4.2.1 Mie Scattering Simulation Background

A significant part of this section of the project involved acquisition of simulation data of Mie scattering for a number of different cluster sizes. This was important for the following reasons:

1. The instrument should be designed to minimise potential measurement interference due to Mie scattering from clusters, which is difficult to distinguish from Rayleigh scattering.
2. As explained in section 5.8, Mie scattering data is essential to extending the instrument's capabilities to allow it to directly measure the presence of clusters in the gas jet.

5.4.2.2 Mie Scattering Simulation Approach

A set of simulations were run for a range of cluster sizes using a multiparticle Mie scattering simulation tool called CELES [43]. This is written in MATLAB and uses NVIDIA CUDA to run the simulation in parallel on graphics hardware. Simulations can still take >1 hr to complete and a computing cluster would be required for full precision simulation with a very large number of particles. CELES requires a file input to set up the simulation – stating particle sizes, refractive indices and coordinates. A custom MATLAB script was developed to generate clusters of N_2 molecules of the required size, to be entered into the simulation. The script had the following responsibilities:

1. CELES works with refractive indices, rather than molecule polarizability. The MATLAB script automatically “converted” molecules into a sphere with the correct size and equivalent refractive index. The script then arranges the refracting spheres into a spherical cluster.

2. The maximum number of particles for a single simulation was 10^4 on the computing power available. However, scattering data was required for clusters of size > 10^6 molecules. The MATLAB script solves this by grouping large numbers of molecules (e.g. 10^3 or 10^5) into a single sphere (with the correct equivalent size/refractive index), and then arranging them in a larger spherical formation to effectively simulate the behaviour of clusters of up to 10^9 molecules (e.g. for 10^9 molecules, 10^4 spheres representing 10^5 molecules each). This approach is justifiable because clusters of up to ~10^5 N_2 molecules are still small enough to only exhibit Rayleigh scattering, and the simulation software will correctly assume that the 10^5-molecule equivalent spheres will simply undergoing Rayleigh scattering as expected.

3. Once CELES has run the simulation, results (angular scattering distributions) are plotted.

Additional details: N_2 polarizability data was from [44], and atomic / cluster packing radii (van der Waals packing) from [45]. An open source geometry generation MATLAB script (“BALL_GRID”) [46] was also used. 20 simulations were run in total, taking on average ~30 minutes each. The simulations were run in Linux with MATLAB r2019a, CUDA 10.0 (gcc compiler) and CELES v2.1.

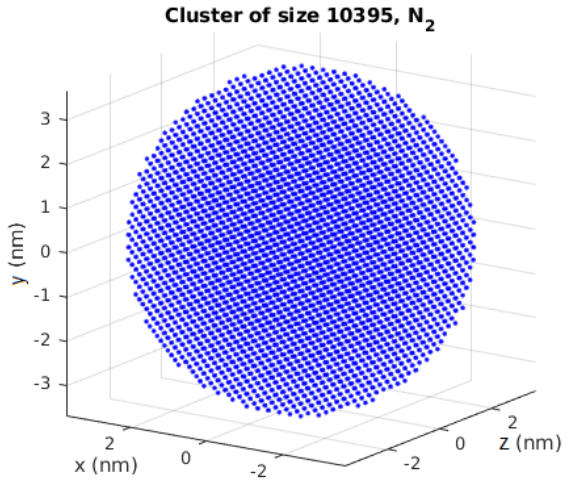

Figure 36: Visualisation of an N_2 cluster of size N=~10^4 produced by custom MATLAB script, for input into CELES to give scattering simulation results.

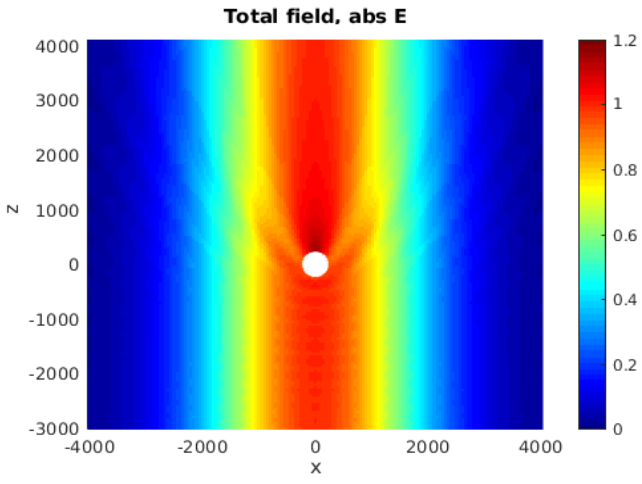

Figure 37: Visualisation of far-field laser light scattering from a large cluster of N_2 molecules – aberrations in the laser beam due to Mie scattering are visible. Output from CELES.

5.4.2.3 Mie Scattering Simulation Results

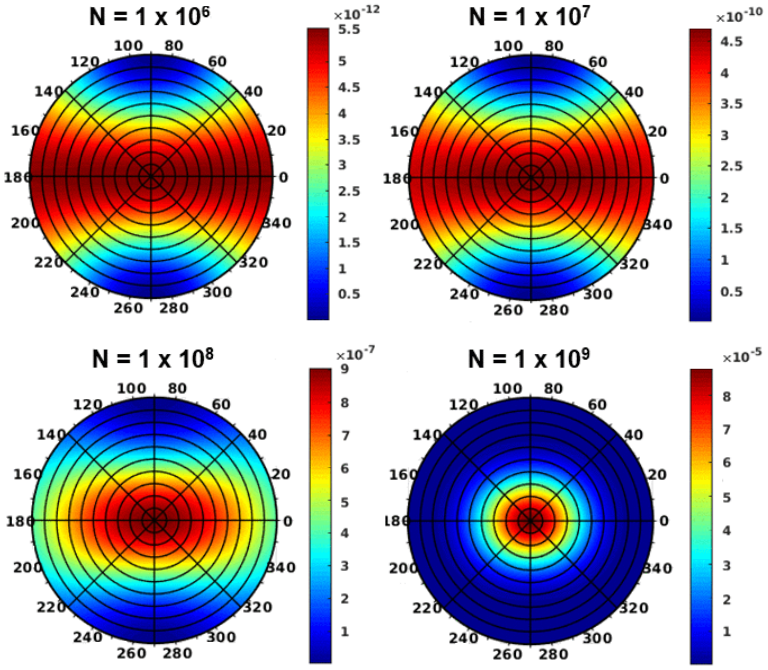

Figure 38: Forward polar view of intensity scattering from clusters of size N. The viewpoint is from the front of the molecule, with laser light from behind.

Figure 38 illustrates the scattering behaviour of simulated N_2 clusters, with N being the number of molecules in the cluster. At $N=10^6$, Rayleigh scattering dominates and energy is radiated almost equally in all directions (on the plane of polarization of the incoming light). As the cluster size increases, more and more energy is radiated purely in the forward direction, until at $N=10^9$ Mie scattering dominates.

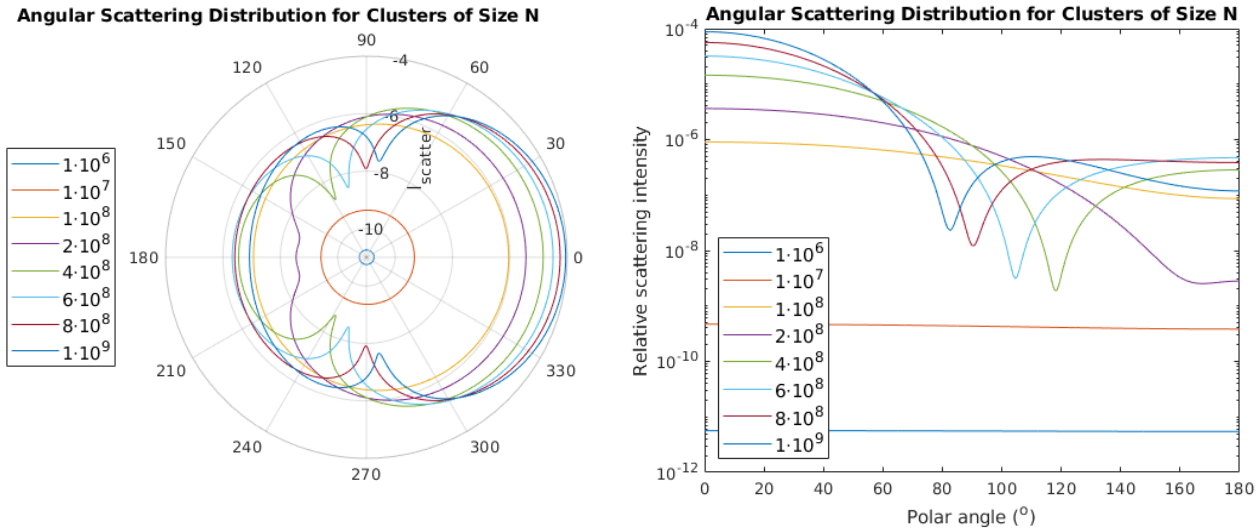

Figure 39: Angular intensity distribution data from simulation. Units are intensity sr^{-1} (logarithmic).

The results show that the minimum of scattered intensity occurs at a ~90° angle from the incoming light. This suggests that, for the optical instrument to minimise interference from strong Mie scattering, the receiver side of the instrument should be at a ~90° scattering angle from the laser. As detailed in section 5.8, Mie scattering intensity distribution data (e.g. from CELES) is also key for the instrument's ability to measure the properties of the clusters in the measurement volume.

5.5 Instrument System Design

5.5.1 Instrument Measurement Uncertainty Characteristic Equation

The core of the optical system design is to maximise the number of received Rayleigh scattered photons from the measurement volume, in order to minimise the statistical measurement uncertainty due to the low number of photons received. Analysis in [41] derived the lower-bound uncertainties for measuring ***ρ, u_k,*** and ***T***, in terms of the number of received Rayleigh scattered photons $\langle N_R \rangle$:

$$\frac{\sigma(\rho)}{\rho} = \left(\frac{1}{\langle N_R \rangle}\right)^{\frac{1}{2}} \qquad \frac{\sigma(u_k)}{a} = \left(\frac{1}{2\langle N_R \rangle}\right)^{\frac{1}{2}} \qquad \frac{\sigma(T)}{T} = \left(\frac{2}{\langle N_R \rangle}\right)^{\frac{1}{2}} \qquad \text{[41]} \quad \text{(Eqn. 19, 20, 21)}$$

$$\langle N_R \rangle = \varepsilon \cdot \frac{P_0 \lambda}{hc} \cdot n L_x \cdot \Delta t \cdot \sin^2 \beta \left(\frac{d\sigma}{d\Omega}\right) \Omega \qquad \text{[41]} \quad \text{(Eqn. 22)}$$

For equation 20: a is the most probable molecular speed. For equation 22: ε is the instrument optical efficiency, P_0 is the laser output power, λ is the laser wavelength, h is Planck's constant, and c is the speed of light. n is the molecule number density (at the measurement volume), and L_x is the length of the measurement volume (assuming that all laser power is focused into the measurement volume). Δt is the time taken for one measurement. β is a polarization/electric field interaction angle ($\sin^2 \beta$ can be assumed to be ≈1 for our purposes), $\left(\frac{d\sigma}{d\Omega}\right)$ is the Rayleigh scattering cross section for the gas species at the laser wavelength (which can be determined either experimentally, or by integrating equation 18 with respect to θ) and Ω is the solid angle of detection for the receiver.

5.5.2 Laser Source Analysis and Choice

A core component of the optical instrument is the coherent laser source, and some in-depth analysis is required to choose an appropriate device. Both continuous-wave (CW) and pulsed lasers can be used for this application, as Rayleigh scattering is a purely linear process and will not saturate with high laser intensity, although most lasers considered here are of the CW variety.

5.5.2.1 Power and Wavelength Optimisation

The two laser-related parameters (laser power P_0 and wavelength λ) appear in equation 18 and equation 22. When $\left(\frac{d\sigma}{d\Omega}\right)$ in equation 22 is replaced by the integral of equation 18, the resulting equation can be rewritten to contain a single group of all laser variables. This group is the laser

suitability group $S = P_0\lambda^{-3}$. This group is effectively a measure of the suitability of a laser source for this application: maximising S will maximise the number of Rayleigh scattered photons, as we require. A representative sample of available lasers was taken based on manufacturers' information available online. A plot of laser output power against wavelength is given in figure 40 for the laser device sample. Also shown are lines of iso-suitability (between S=10^{18} and S=10^{21} – any two lasers that are plotted the same vertical distance from an iso-line should perform identically in the instrument. Clearly, a shorter-wavelength laser will be more suitable than a longer-wavelength laser of the same power – due to the fact that Rayleigh scattering is so strongly wavelength dependent.

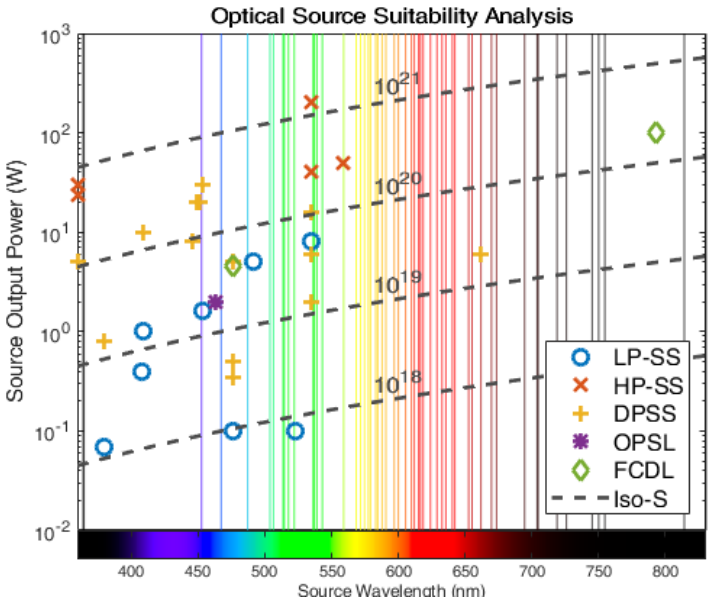

Figure 40: Output power against wavelength plot for lasers available, with iso-contours of suitability value S.

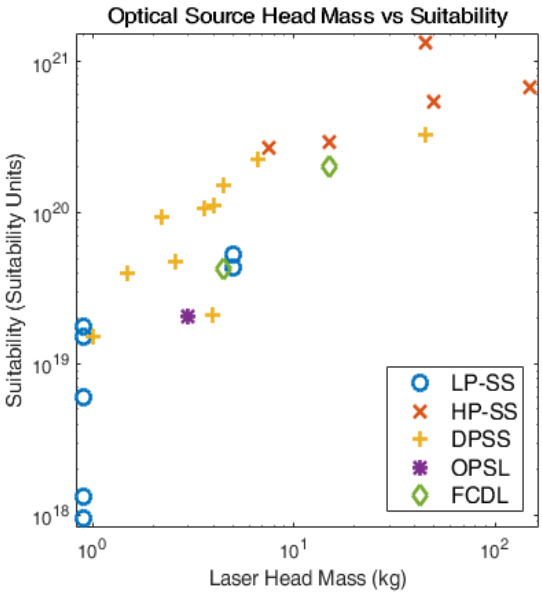

Figure 41: General trend of increasing suitability value increasing the laser mass.

The key for each graph gives the laser type: Low-Power and High-Power Solid State (LP-SS and HP-SS), Diode-Pumped Solid-State (DPSS), Optically Pumped Semiconductor Laser (OPSL), and Fibre-Coupled Diode Lasers (FCDL).

5.5.2.2 Power and Mass Considerations

As shown in figure 41, there is a strong positive correlation between the laser suitability and its mass. Mass is also strongly linked to power/cooling requirements and safety issues – all things that should be minimised. The most "suitable" HP-SS laser has an output power of 200 W and requires liquid cooling. Overall, there are several serious drawbacks to using a very high-power laser.

5.5.2.3 Gas Species Absorption Considerations

It is important to ensure that the laser wavelength is not near a photon absorption peak for the gas species used – if photons are absorbed and re-emitted they will be indistinguishable from Rayleigh scattered photons and hence will interfere with the measurement. Also, as discussed in section 4.4.4, absorption peaks introduce the possibility for the gas to absorb kinetic energy from the laser.

Nitrogen is a simple gas species to design for – it does not absorb photons at all in the 300 nm - 800 nm range [47]. However, working with neon is significantly more difficult as it has a number of absorption peaks throughout the visible spectrum [48] – these are shown in figure 40. These lines preclude the usage of many lasers, especially the large number of research-grade lasers at 532 nm.

5.5.2.4 Coherence Length

For interferometry on the receiver side (section 5.6.3), a coherence length (the spatial length over which the laser light is coherent) needs to be on the order of a few cm. However, in most HP-SS and many DP-SS lasers, many laser diodes are combined to increase the output power. This results in the output light not being coherent enough for our requirements.

5.5.2.5 Laser Source Choice

Taking into account laser head mass, cost and interoperability between neon and nitrogen, a semiconductor solid-state laser at 405 nm / 1.2 W was chosen as the best candidate - a specific example is the Frankfurt Laser Company FVLD-405-1200M [49]. This laser has a lower suitability rating than several HP-SS lasers, but it is far enough from a neon absorption line, should be coherent enough (as a single-emitter semiconductor laser), and has a sensible output optical power. 405 nm is also at the edge of the visible light spectrum: using a lower wavelength and non-visible laser beam would involve more risk and require more safety precautions. The laser diode would be deemed a Class 4 laser (the most dangerous class of laser) by IEC 60825-1, due to its high output power. There are several design and operation considerations required to minimise this risk:

1. The laser should only be at its highest power at the focal point, inside the gas apparatus. The interior should be coated with black anti-reflective paint, which should act as a beam dump.
2. General laser safety approaches – training, eye protection, interlocks, visible warnings, etc.

5.6 Instrument Detail Design

5.6.1 Laser Focusing and Diode Output Collimation

Gaussian beam optics are used to consider the focus of the laser onto the measurement volume [50]. To deliver close to 100% of the laser power into a cross section of (0.1 mm)^2, the Gaussian radius ω_0 of the focal point should be ~0.025 mm (rather than ~87% of power with $\omega_0 = 0.05$ mm). To find the diameter D of the collimated beam input to the focal optic:

$$2\omega_0 = \left(\frac{4\lambda}{\pi}\right)\frac{f}{D} \quad [50] \quad \text{(Eqn. 23)} \qquad f = \frac{r}{\tan\left(\frac{\theta}{2}\right)} \quad [51] \quad \text{(Eqn. 24)}$$

With a focusing lens with f = 300.0 mm (so that the focal point can be placed up to ~300 mm into the gas apparatus) this gives a desired laser beam diameter of 3 mm. The FVLD-405-1200M laser diode has a diverging beam output that requires collimation. For this diode, θ_{fast} = 40° and θ_{slow} = 22°. The most suitable method of forming a near-circular beam from this output is with two cylindrical lenses [52]. Equation 24 gives the required focal length for each cylindrical lens (taking into account the closest off-the-shelf lenses available): f_{fast} = 4.0 mm and f_{slow} = 10.0 mm. This choice of lenses also takes into account how the lenses can be placed to give enough clearance relative to each other and the laser diode. This combination gives a slightly elliptical beam of nominal diameter ~3.1 mm.

5.6.2 Laser Source Side Design Proposal

The CAD assemblies below made use of several freely available CAD models from Thorlabs [53].

ID	Component	Function / Description
1	405 nm 1200 mW TO laser diode in temperature-controlled mount.	Mounts and powers the laser diode and keeps its temperature (and hence output spectrum) constant.
2	2 x cylindrical lens beam collimator for 3 mm diameter.	Provides beam collimation in both axes independently, for a ~3 mm diameter output beam.
3	Beam focus lens, *f* = 300.0 mm.	Focuses the laser onto the measurement volume inside the gas apparatus.
4	Focus lens linear translation stage, 0 – 150 mm.	Allows the focal point to be adjusted along the laser beam line, for moving the measurement volume.
5	Laser steering 2-axis mirror galvanometer.	Allows the laser beam to be steered to focus on any measurement volume in the viewport solid angle.
6	Gas apparatus laser-in viewport.	The gas apparatus viewport that laser light enters through. Should be anti-reflection coated for 405 nm.

Table 8: Design breakdown for laser source side of the instrument.

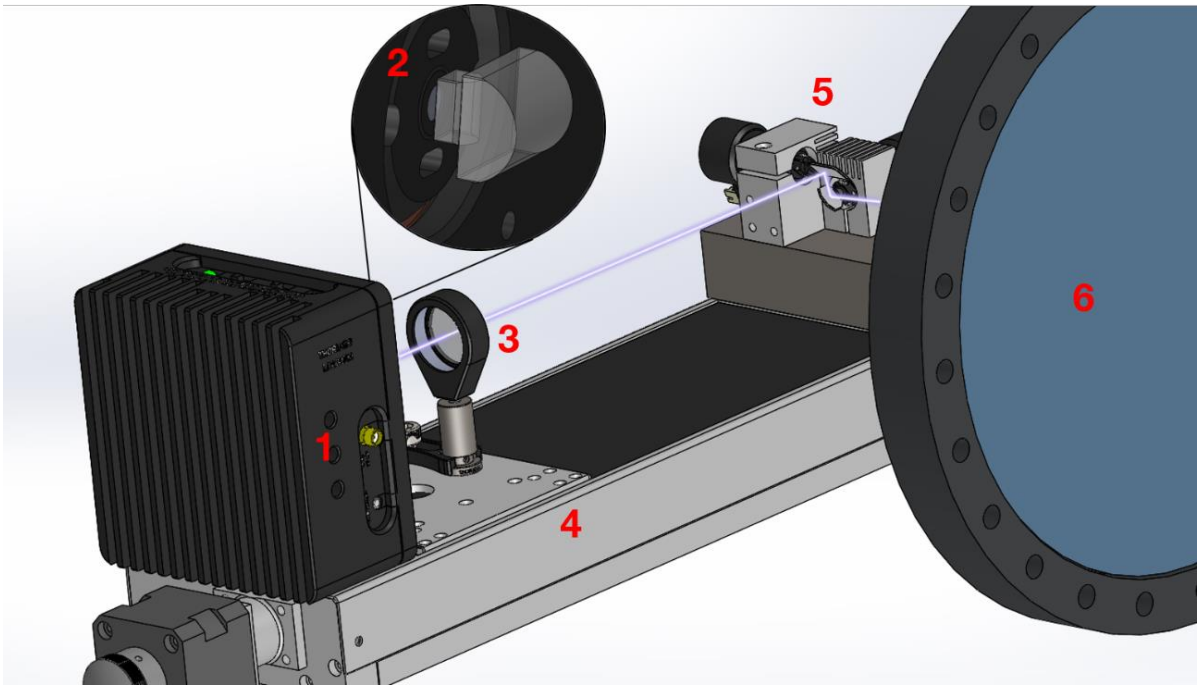

Figure 42: CAD assembly model of the proposed laser side design for the instrument.

5.6.3 Photon Detector Side Design Proposal

The function of this side of the instrument is to receive photons that are scattered from the measurement volume, and redirect them into a Fabry-Perot interferometer for spectral analysis.

ID	Component	Function / Description
1	Gas apparatus scattering-out viewport.	As discussed in section 5.4.2.3, this viewport should be perpendicular / 90° to the laser-in viewport.
2	Scattered photon redirection 2-axis mirror galvanometer.	Redirects photons scattered from the measurement volume. Standard mirror galvanometers have a small enough repeatability to be able to accurately point at $(0.1\ \text{mm})^3$ volumes 300 mm away (<300 μradians).
3	Field of view focus lens, f = 300.0 mm.	Ensures only photons from the measurement volume are collected by focusing on it.
4	Field of view focus lens linear translation stage, 0 – 150 mm.	Allows the effective focal point to be adjusted onto the measurement volume.
5	Fabry-Perot interferometer alignment lens, f = 200.0 mm.	Redirects incoming photons to focus them onto the focal plane of the FPI.
6	Scanning Fabry-Perot interferometer (FPI).	As in [41], an FPI is used to determine the frequency of incoming photons. A scanning FPI only allows photons of a specific frequency wavelength through to the sensor, and a non-scanning FPI redirects photons of different wavelengths to multiple sensors.
7	Amplified / avalanche photodetector.	Photon detection – needs to be very high sensitivity due to the small number of incoming photons.

Table 9: Design breakdown for photon detection side of the instrument.

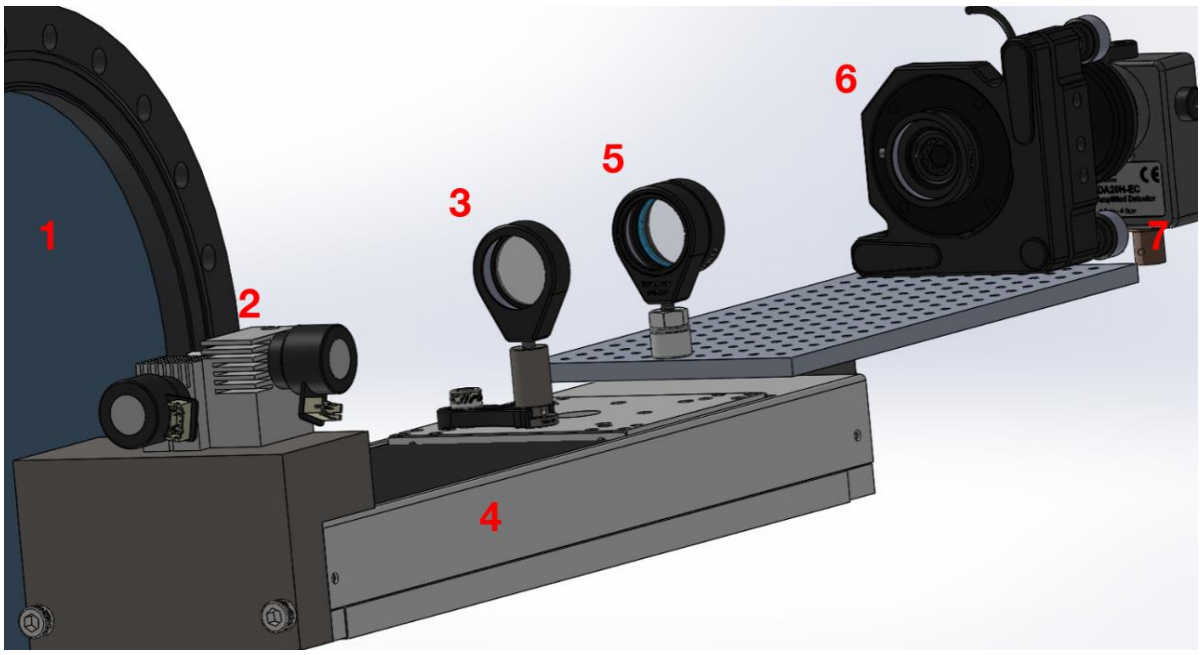

Figure 43: CAD assembly model of the proposed detector side design for the instrument.

5.7 Design Performance Analysis

5.7.1 Instrument Characterisation and Measurement Time Estimates

Variable	Value	Source / Justification
ε	0.227	Combination of 5 x lens (ε=0.95), 4 x mirror (ε=0.99), 2 x viewport (ε=0.92), photodetector (ε=0.4) and FPI (ε=0.9).
P_0	1.2 W	Section 5.5.2.5 (Laser Source Choice)
λ	405 nm	Section 5.5.2.5 (Laser Source Choice)
n	2.46 x 10^{20} to 2.5 x 10^{16}	Converted from R5.2 – range of working densities.
L_x	0.1 mm or 1 mm	High-resolution or low-resolution scan, from R5.6.
$\left(\frac{d\sigma}{d\Omega}\right)$	N_2: 1.71x10^{-30} m^2 Ne: 7.15 x 10^{-32} m^2	Interpolated between wavelength values in absolute cross-section tables in [54], to find the 405 nm value.
Ω	4.9 x 10^{-4} sr	Calculated from the area of the galvanometer mirrors.

Table 10: Values used to estimate performance of optical state characterisation instrument.

Using equation 22 to estimate the number of received photons per second gives the following table. Also shown are the measurement times per mm^3 given the uncertainty requirements (largest number required is 400 photons per density reading (for 5% uncertainty, according to equation 19).

	Highest density (near nozzle) – $(0.1mm)^3$		Lowest density – $1mm^3$.	
N_2	11.47 s^{-1}	~3.49 x 10^4 s per mm^3	1.165 x 10^{-3} s^{-1}	~3.4 x 10^4 s per mm^3
Ne	0.479 s^{-1}	~8.35 x 10^5 s per mm^3	4.87 x 10^{-5} s^{-1}	~8.21 x 10^5 s per mm^3

Table 11: Expected photon arrival rates and corresponding measurement times.

For this table, it is assumed that the areas of most interest (around the nozzle and first skimmer, with high gas density) would be measured with the fine $(0.1\ \text{mm})^3$ per measurement volume scan, and the low-density parts of the gas jet that are less important are measured with a $1\ \text{mm}^3$ scan. The $(0.1\ \text{mm})^3$ scan will be ~10000x slower than the $1\ \text{mm}^3$ scan (simply by having to carry out 1000x as many measurements per mm, with 10x smaller photon rate per measurement) but this is partly offset by the increased gas density at the points of interest. This also assumes that a non-scanning FPI is used – a scanning FPI will take a significant factor longer as it has to scan through all wavelengths.

5.7.2 Possible Improvements to Current Design

The measurement times calculated are reasonable given the small volume of the gas jet that needs measuring. However, one straightforward way to increase the speed of measurements would be to increase the solid angle of reception by increasing the size of the galvanometer mirrors and lenses. This could easily increase the solid angle (and hence the photon rate) by a factor of 10 – 100.

5.8 Extension to Cluster Detection/Analysis via Mie Scattering

An approach given in [55] can be used to characterise clusters of molecules in the measurement volume using the dependence of the Mie scattering angular intensity distribution on particle size.

$I(\theta) = F(\theta, x)q(x)$ [55] (Eqn. 25) $q = (F^T F + \gamma E)^{-1} F^T I$ [55] (Eqn. 26)

The scattering particle size parameter $x = \frac{2\pi r}{\lambda}$, where *r* is the scattering particle radius. $q(x)$ is the size distribution of clusters in the measurement volume, and $I(\theta)$ is the angular intensity distribution, recorded by photon detectors at multiple angles. $F(\theta, x)$ is the "scattering coefficient" matrix with the row index being scattering angle values, and the column index being x-parameter values. This matrix is computed, for example with CELES (section 5.4.2), for a large number of values of x and θ.

Equation 25 shows how the angular intensity matrix is a formed from the particle size distribution and the scattering matrix that gives the angular intensity distribution for each size of particle.
One method to recover the cluster size distribution is given by equation 26, which uses non-negative least squares with regularisation to recover a numerically stable estimate for $q(x)$.

6 CONCLUSIONS AND POSSIBLE FURTHER WORK

6.1 Compressible Flow

6.1.1 Conclusions

In section 2, the laws and applications of compressible flow were explored. The initial one-dimensional dimensionless approach discovered that with increased area ratio, downstream density increases. However, Mach number decreases, and vice versa for decreased area ratio. This led to the finding that when designing a CD nozzle, it can be understood as a trade-off between Mach number and density.

It was then suggested that another priority should be having parallel stream lines coming out of the nozzle. The one-dimensional equations showed that a very large area ratio would be required to achieve this. It was then contextualised with the parameters set out in the constraint (section 2.1.2) and it was shown that the value for the nozzle exit diameter produced was feasible.

A further feasibility study was done for this nozzle using CFD software. Here the nozzle was studied using various flow regimes, all producing similar results to the ones shown (figures 13-17). Many of the results varied from the results of the one-dimensional equations, most notably Mach number. It was then shown that this was not due to a low horizontal velocity but in fact due to a significantly higher than expected temperature.

The CFD software also showed a lot of separation from the walls, but as indicated, it did not affect the flow into the skimmer, so in theory has minimal adverse effect on the aim of having parallel streamlines into the first skimmer.

The results were compared to that of an independent research group at the University of Wroclaw [15] showing similar results. This supports the validity of the results in this study. The results here did yield a significantly larger density and hence seem to be a promising route for further study.
It is however impossible to get away from the fact that there are consistent variations between the one-dimensional equations, the compressible flow CFD solver, and the small pool of numerical data found in the literature. For this reason, the Knudsen number was revisited and applied to all three of

these cases. These all produced values for Knudsen number that were not indicative of compressible flow, and hence possibly the reason for variations in solutions.

In summary; this section shows the struggles of applying the laws of compressible flow near the boundary at which compressible flow breaks down, shown by the values of Knudsen number. It does, however, show significant evidence that a CD nozzle with a throat diameter of 30 μm and exit diameter of 4.8 mm could provide significant improvements to the current system.

6.1.2 Further work

In section 2.1 the constraints were laid out, including the decision to use nitrogen alone. This project therefore has scope to also investigate the suitability of neon, or any other proposed working gas. To investigate the boundary between compressible flow and molecular flow, Knudsen number alone was used. Within this, only one method of calculating Knudsen number was cited [13]. Further work could therefore be implemented to better understand the drivers of Knudsen number with the use of other sources. A study into other methods of defining the boundary between compressible flow and molecular flow could also have been undertaken.

Equations 3 and 4 were the basis for defining the geometry of the nozzle that was proposed. However, these equations have many assumptions, more than just compressible flow. Further work could therefore involve challenging these assumptions further and trying to understand what effect breaking one of these assumptions would have.

The ANSYS Fluent model was only for a two-dimensional cross-section. As shown through the unintuitive existence of vertical velocity when computing both halves of the nozzle, rather than one half, computing the full three-dimensional nozzle might have yielded more interesting results. Given more simulation run-time – therefore allowing a finer mesh – would have also been beneficial, especially focusing it along the central column of the nozzle as this would provide a higher resolution in the central 200 μm exit of the nozzle. Applying CFD to the nozzle and first chamber together would have been interesting, as this would give a better understanding of the flow in the first chamber, rather than just having to rely on the assumptions of the design condition nozzle.

ANSYS Fluent was not the ideal software for this task. This was highlighted when Knudsen number indicated that the flow was not compressible flow from the results of the CFD model, even though ANSYS describes its software as a compressible flow solver. This is highlighted by the fact that Fluent only deals in gauge pressure from atmospheric, making it challenging to achieve the exact exit pressure of 0.1Pa. Possible further work could therefore be to design a software package that merges compressible flow relations with that of molecular flow when required. For example, discussing the possibility with ANSYS for them to integrate Molflow into one of their compressible flow solvers.

6.2 Undesirable Flow Effects

6.2.1 Conclusions

In section 3 research was carried out to understand more about the formation of condensation and clusters as they might cause damage to the equipment.

From looking at the phase diagrams it was clear that the 60 K was not an issue for either working gas. The 10 K result was within the solid phase region of the phase diagrams for both working fluids however it was much further to from the saturation line. The 3 K temperature was clearly very far from the saturation line and would require expert use of a phenomenon to avoid condensation at that temperature.

The phenomenon that can be used to avoid the condensation at temperatures below equilibrium saturation pressure is supercooling. Supercooling only occurs when the nozzle has a high expansion rate – our nozzle has a very high expansion rate which means that there will be a high degree of supercooling. From the phase diagrams it is apparent that the 10 K can be achieved without condensation and that it might be possible for 3 K.

For cluster formation there are empirical equations which help determine the size of the clusters. To accurately determine the value of the reduced Hagena parameter and therefore the cluster size, a scaling value is required which would need to be derived experimentally.

6.2.2 Further work

This would require finding more information such as the scaling parameter, q, from experiments to then have a more accurate value of the scaled Hagena parameter. For the condensation side of the project more work could be done to see if there are other similarities between neon and nitrogen. More work could also be done to find more values with higher expansion rates to complement figure 24, this would give more data and therefore offer better lines for extrapolation.

6.3 Molecular Flow Analysis

6.3.1 Conclusions

In section 4 a simulation program was developed from molecular flow and kinetic theory, was validated using literature data and proved to be useful for examining the behaviour of the gas apparatus. This made use of the outputs of the viscous flow modelling in section 2.3.2, and enabled links to be made between the viscous flow side and the performance of the gas curtain. The results suggested that gas curtain homogeneity could be improved by adjusting skimmer placement or by increasing the input temperature, e.g. with a heated nozzle. However, this would lower the proportion of molecules that reach the curtain and increase thermal motion measurement uncertainty.

6.3.2 Further Work

Further work on this section could involve carrying out a more in-depth comparison between the previous results from Molflow and the results from this model, and investigating any discrepancies. Further work could also take place to fully implement the ability for the model to simulate the behaviour/end effect of cluster transport along the gas jet. This would require more literature review and research e.g. to find a model of how the clusters break up as they travel along the gas jet.

6.4 Optical Gas Jet Characterisation Instrument

6.4.1 Conclusions

Section 5 showed that an optical instrument would be an effective way to solve the computational gas flow modelling problems experienced by CERN, by validating the models experimentally.

The analysis shows that an instrument based on Rayleigh scattering could feasibly be used to experimentally measure molecular gas jets in any low-pressure gas apparatus, including the gas curtain formation apparatus used by the gas curtain beam profile monitor. This approach can simultaneously measure all variables of interest, including determining whether clusters are affecting the performance of the gas apparatus. The instrument design made extensive use of analysis of the gas jet flow from sections 2 and 4. Analysis of the final instrument design proposal showed that it should be capable of achieving all of its design requirements with a reasonable measurement time,

and a fine enough volumetric resolution compared to the small skimmer and nozzles geometries.

6.4.2 Further work

Further work on this area could involve more in-depth design of the instrument, for integration with the prototype gas apparatus at Cockcroft. This would take into account gas apparatus dimensions and where the available viewports are situated for access to each section of the flow.

6.5 Overall Project Conclusions

This 3rd Year Project carried out an in-depth analysis of the gas apparatus that produces the beam gas curtain for particle beam profile measurement. The scope of this project was decided after an extensive literature review on the subject and consultation with CERN about the areas of the Beam-Induced Fluorescence profile measurement approach they would like to have more information on.

The project involved analysis of both the viscous flow and molecular flow regimes, including looking at non-ideal flow effects that could have an impact on the gas jet/curtain performance. This analysis and data (from theory and simulation) gives CERN more information in several areas of gas apparatus design. It also validates CERN's concerns about the performance of computational gas flow models.

Several design recommendations were also made for improving the performance of the gas curtain. These results were based on design analysis of the nozzle and modelling of the geometries and locations of the skimmers that collimate and shape the gas jet.

A high-level design for an experimental instrument was proposed that would be suited to measuring the gas jet in the gas apparatus. This is of interest to CERN as they want their computer models of the gas flow validated to ensure that the gas apparatus is behaving as expected. The instrument design proposed is flexible and could potentially be used for a number of different experiments involving low-density gas flows, with only minor modifications to the optical focusing system.

The results of this project were presented to engineers and researchers at CERN on 23/04/2019.

APPENDIX: REFERENCES

[1] Online resource: home.cern/science/accelerators/high-luminosity-lhc - retrieved 08/04/2019.

[2] Online resource: home.cern/resources/faqs/high-luminosity-lhc - retrieved 08/04/2019.

[3] Sirvent Blasco, J.L., Roncarlo, F., Dehning, B., & Dieguez, A. (2018). Beam secondary shower acquisition design for the CERN high accuracy wire scanner. http://cds.cern.ch/record/2640438

[4] Forck, P., Andre, C., Becker, F., Haseitl, R., & Walasek-Höhne, B. (2010). Beam induced fluorescence profile monitor developments. In HB 2010 - 46th ICFA Advanced Beam Dynamics Workshop on High-Intensity and High-Brightness Hadron Beams (pp. 497–501). Retrieved from https://www.scopus.com/inward/record.uri?eid=2-s2.0-84884390637&partnerID=40&md5=e23a88e09353079c4e9bd08bc828b2ea

[5] Tzoganis, V., Jeff, A., & Welsch, C. P. (2014). Gas dynamics considerations in a non-invasive profile monitor for charged particle beams. Vacuum, 109, 417–424. https://doi.org/10.1016/j.vacuum.2014.07.009

[6] Zhang, H., Tzoganis, V., Jeff, A., Alexandrova, A., & Welsch, C. P. (2016). Characterizing supersonic gas jet-based beam profile monitors. In IPAC 2016 - Proceedings of the 7th International Particle Accelerator Conference (pp. 357–360). Retrieved from https://www.scopus.com/inward/record.uri?eid=2-s2.0-85015272044&partnerID=40&md5=103e289973f1bb3f7dc5c0c6e86cf613

[7] Tzoganis, V., Zhang, H. D., Jeff, A., & Welsch, C. P. (2017). Design and first operation of a supersonic gas jet based beam profile monitor. Physical Review Accelerators and Beams, 20(6), 062801. https://doi.org/10.1103/PhysRevAccelBeams.20.062801

[8] Online resource: www.home.cern/about/who-we-are/our-mission - retrieved 22/02/2019.

[9] Ady, Marton M. “Re: Oxford CERN 3YP.” Message to Daniel Eakins. 29 November 2019. E-mail.

[10] Beardsley. Mat M. “Re: Nozzle Commissioning Enquiry.” Message to Ben Brown. 04 February 2019. E-mail.

[11] Online resource: www.kayelaby.npl.co.uk/general_physics/2_2/2_2_4.html - retrieved 24/04/2019.

[12] p. 75: M. Howatson, A., G. Lund, P., & D. Todd, J. (1972). Engineering Tables and Data. https://doi.org/10.1007/978-94-010-9314-9

[13] Online resource: www.pfeiffer-vacuum.com/en/know-how/introduction-to-vacuum-technology/fundamentals/mean-free-path/ - retrieved 27/04/2019.

[14] Online resource: www.sciencedirect.com/topics/engineering/knudsen-number - retrieved 27/04/2019.

[15] Online resource: https://indico.cern.ch/event/712498/contributions/2926528/attachments/1619269/2575222/Nozzle_HighPressure_BGCMeeting_PS.pdf - retrieved 27/04/2019.

[16] Douglas, J., Gasiorek, J., Swaffield, J., Jack, L., Fluid Mechanics, Pearson, 2005 fifth edition (equation 1.13)

[17] Douglas, J., Gasiorek, J., Swaffield, J., Jack, L., Fluid Mechanics, Pearson, 2005 fifth edition (equation 13.1)

[18] Douglas, J., Gasiorek, J., Swaffield, J., Jack, L., Fluid Mechanics, Pearson, 2005 fifth edition (equation 5.31)

[19] Online resource: en.wikipedia.org/wiki/Rocket_engine_nozzle#/media/File:Rocket_nozzle_expansion.svg

[20] Online resource: www.engapplets.vt.edu/fluids/CDnozzle/cdinfo.html

[21] Papamoschou, D., Zill, A., & Johnson, A. (2008). Supersonic flow separation in planar nozzles. Shock Waves, 19(3), 171. https://doi.org/10.1007/s00193-008-0160-z

[22] Bourgoing, A., & Reijasse, P. (2005). Experimental analysis of unsteady separated flows in a supersonic planar nozzle. Shock Waves, 14(4), 251–258. https://doi.org/10.1007/s00193-005-0269-2

[23] Online Resource: https://www.chemguide.co.uk/physical/phaseeqia/phasediags.html retrieved 12/04/19

[24] Online Resource: https://encyclopedia.airliquide.com/nitrogen retrieved 12/04/19

[25] Online Resource: https://encyclopedia.airliquide.com/neon retrieved 12/04/19

[26] Grossir, G. (2015). Longshot Hypersonic Wind Tunnel Flow Characterization and Boundary Layer Stability Investigations. https://doi.org/10.13140/RG.2.1.2394.0720

[27] Online resource: https://www.chemguide.co.uk/atoms/bonding/vdw.html retrieved on 09/05/19

[28] Hagena, O. F. (1987). Condensation in free jets: Comparison of rare gases and metals. Zeitschrift Für Physik D Atoms, Molecules and Clusters, 4(3), 291–299. https://doi.org/10.1007/BF01436638

[29] Tzoganis, V., Jeff, A., & Welsch, C. P. (2014). Gas dynamics considerations in a non-invasive profile monitor for charged particle beams. Vacuum, 109, 417–424. https://doi.org/10.1016/j.vacuum.2014.07.009

[30] Online resource: www.pfeiffer-vacuum.com/en/know-how/introduction-to-vacuum-technology/fundamentals/types-of-flow/ - retrieved 01/05/2019.

[31] Online resource: https://molflow.web.cern.ch/content/about-molflow - retrieved 30/04/2019.

[32] Zhang, H., Tzoganis, V., Jeff, A., Alexandrova, A., & Welsch, C. P. (2016). Characterizing supersonic gas jet-based beam profile monitors. In IPAC 2016 - Proceedings of the 7th International Particle Accelerator Conference (pp. 357–360). Retrieved from https://www.scopus.com/inward/record.uri?eid=2-s2.0-85015272044&partnerID=40&md5=103e289973f1bb3f7dc5c0c6e86cf613

[33] Cached online resource: web.archive.org/web/20170517032951/http://www-thphys.physics.ox.ac.uk/people/PeterConlon/notes/kinetictheory.pdf - last captured on 17/05/2017.

[34] Online resource: en.wikipedia.org/wiki/Maxwell–Boltzmann_distribution - retrieved 04/02/2019.

[35] Online resource: hyperphysics.phy-astr.gsu.edu/hbase/Kinetic/kintem.html – retrieved 04/02/2019.

[36] Tzoganis, V., & Welsch, C. P. (2014). A non-invasive beam profile monitor for charged particle beams. Applied Physics Letters, 104(20). https://doi.org/10.1063/1.4879285

[37] Online resource: physics.nist.gov/cgi-bin/Compositions/stand_alone.pl – retrieved 04/02/2019.

[38] Welsch, C. (2010). Numerical studies of curtain gas jet generation for beam profile monitoring applications in the ultra low energy storage ring. 2010 Beam Instrumentation Workshop, BIW 2010 - Proceedings.

[39] Metcalf, H. J., & van der Straten, P. (2003). Laser cooling and trapping of atoms. J. Opt. Soc. Am. B, 20(5), 887–908. https://doi.org/10.1364/JOSAB.20.000887

[40] Eckbreth, A. C. (1981). Recent advances in laser diagnostics for temperature and species concentration in combustion. Symposium (International) on Combustion, 18(1), 1471–1488. https://doi.org/10.1016/S0082-0784(81)80150-6

[41] Seasholtz RG, Panda J, Elam KA (2002). Rayleigh scattering diagnostic for measurement of velocity and density fluctuation spectra. AIAA-2002-0827

[42] Online resource: hyperphysics.phy-astr.gsu.edu/hbase/atmos/blusky.html – retrieved 03/05/2019.

[43] Egel A, Pattelli L, Mazzamuto G, Wiersma DS, and Lemmer U. CELES: CUDA-accelerated simulation of electromagnetic scattering by large ensembles of spheres, Journal of Quantitative Spectroscopy and Radiative Transfer 199C (2017) pp. 103-110.

[44] Online resource: cccbdb.nist.gov/exp2x.asp?casno=7727379&charge=0 – retrieved 09/04/2019.

[45] Online resource: wikipedia.org/wiki/Atomic_radii_of_the_elements_(data_page) – retrieved 09/04/19.

[46] Online resource: people.sc.fsu.edu/~jburkardt/m_src/ball_grid/ball_grid – retrieved 10/04/2019.

[47] Lofthus, A., & H. Krupenie, P. (1977). The spectrum of molecular nitrogen. Journal of Physical and Chemical Reference Data - J PHYS CHEM REF DATA, 6, 113–307. https://doi.org/10.1063/1.555546

[48] NIST Atomic Spectra Database (ver. 5.6.1), [Online]. Available: https://physics.nist.gov/asd [2019, March 28]. National Institute of Standards and Technology, Gaithersburg, MD. DOI: https://doi.org/10.18434/T4W30F

[49] Online resource: www.frlaserco.com/uploads/files/20160209125143_FVLD-405-1200M.pdf - retrieved 13/04/2019.

[50] Online resource: www.newport.com/n/gaussian-beam-optics - retrieved 13/04/2019.

[51] Online resource: www.edmundoptics.com/resources/application-notes/optics/what-are-cylinder-lenses/ - retrieved 13/04/2019.

[52] Online resource: www.thorlabs.com/images/TabImages/Elliptical_Beam_Circularization_Lab_Fact.pdf - retrieved 13/04/2019.

[53] Online resource: www.thorlabs.com/navigation.cfm – retrieved 03/05/2019.

[54] SHARDANAND & D. P. Rao, A. (1977). Absolute Rayleigh scattering cross sections of gases and freons of stratospheric interest in the visible and ultraviolet regions.

[55] Jinno, S., Tanaka, H., Matsui, R., Kanasaki, M., Sakaki, H., Kando, M., … Fukuda, Y. (2017). Characterization of micron-size hydrogen clusters using Mie scattering. Opt. Express, 25(16), 18774–18783. https://doi.org/10.1364/OE.25.018774